NF1 regulates mesenchymal glioblastoma plasticity and aggressiveness through the AP-1 transcription factor FOSL1

Carolina Marques[1], Thomas Unterkircher[2], Paula Kroon[1], Annalisa Izzo[2], Gaetano Gargiulo[3], Eva Kling[2], Oliver Schnell[2], Sven Nelander[4], Erwin F. Wagner[5,6,7], Latifa Bakiri[5,7], Maria Stella Carro[2*] and Massimo Squatrito[1*]

[1]Seve Ballesteros Foundation Brain Tumor Group, Spanish National Cancer Research Centre, CNIO, 28029 Madrid, Spain.
[2]Department of Neurosurgery, Faculty of Medicine Freiburg, D-79106 Freiburg, Germany.
[3]Max-Delbrück-Center for Molecular Medicine (MDC), Robert-Rössle-Str. 10, 13092 Berlin, Germany.
[4]Dept of Immunology, Genetics and Pathology and Science for Life Laboratory, Uppsala University, Rudbecklaboratoriet, SE-751 85 Uppsala, Sweden.
[5]Genes, Development, and Disease Group, Spanish National Cancer Research Centre, CNIO, 28029 Madrid, Spain.
[6]Dermatology Department, Medical University of Vienna, A-1090 Vienna, Austria.
[7]Laboratory Medicine Department, Medical University of Vienna, A-1090 Vienna, Austria.

* Correspondence: maria.carro@uniklinik-freiburg.de; msquatrito@cnio.es

Lead contact: Massimo Squatrito

Summary

The molecular basis underlying Glioblastoma (GBM) heterogeneity and plasticity are not fully understood. Using transcriptomic data of patient-derived brain tumor stem cell lines (BTSCs), classified based on GBM-intrinsic signatures, we identify the AP-1 transcription factor *FOSL1* as a master regulator of the mesenchymal (MES) subtype. We provide a mechanistic basis to the role of the Neurofibromatosis type 1 gene (*NF1*), a negative regulator of the RAS/MAPK pathway, in GBM mesenchymal transformation through the modulation of *FOSL1* expression. Depletion of *FOSL1* in NF1-mutant human BTSCs and Kras-mutant mouse neural stem cells results in loss of the mesenchymal gene signature, reduction in stem cell properties and *in vivo* tumorigenic potential. Our data demonstrate that *FOSL1* controls GBM plasticity and aggressiveness in response to *NF1* alterations.

Keywords

GBM, Mesenchymal, NF1, FOSL1, FRA-1, master regulator

Significance

Glioblastoma (GBM) is a very heterogenous disease for which multiple transcriptional subtypes have been described. Among these subtypes, the Mesenchymal (MES) GBMs have the worst prognosis. Here we provide the first causal evidence linking Neurofibromatosis type 1 gene (NF1) signalling and the acquisition of a MES gene expression program through the regulation of the AP-1 transcription factor *FOSL1*. Using patient expression datasets, combined with *in vitro* and *in vivo* gain- and loss- of function mouse models, we show that *FOSL1* is an important modulator of GBM that is required and sufficient for the activation of a MES program. Our work sheds light on the mechanisms that control the tumorigenicity of the most aggressive adult brain tumor type.

Introduction

Glioblastoma (GBM), the most common and aggressive primary brain tumor in adults, is characterized by high molecular and cellular inter- and intra-tumoral heterogeneity. Large-scale sequencing approaches have evidenced how concurrent perturbations of cell cycle regulators, growth and survival pathways, mediated by RAS/MAPK and PI3K/AKT signaling, play a significant role in driving adult GBMs (Brennan et al., 2013; The Cancer Genome Atlas Research Network, 2008; Verhaak et al., 2010). Moreover, various studies have classified GBM in different subtypes, using transcriptional profiling, being now the Proneural (PN), Classical (CL) and Mesenchymal (MES) the most widely accepted (Phillips et al., 2006; Verhaak et al., 2010; Wang et al., 2017).

Patients with the MES subtype tend to have worse survival rates compared to other subtypes, both in the primary and recurrent tumor settings (Wang et al., 2017). The main driver genetic alteration – Neurofibromatosis type 1 gene (*NF1*) copy number loss or mutation – and important regulators of the MES subtype, such as STAT3, CEBPB and TAZ, have been identified (Bhat et al., 2011; Carro et al., 2010; Verhaak et al., 2010). Nevertheless, the mechanisms of regulation of MES GBMs are still not fully understood. For example, whether the MES transcriptional signature is controlled through tumor cell-intrinsic mechanisms or influenced by the tumor microenvironment (TME) is still an unsolved question. In fact, the critical contribution of the TME adds another layer of complexity to MES GBMs. Tumors from this subtype are highly infiltrated by non-neoplastic cells, as compared to PN and CL subtypes (Wang et al., 2017). Additionally, MES tumors express high levels of angiogenic markers and exhibit high levels of necrosis (Cooper et al., 2012).

Even though each subtype is associated with specific genetic alterations, there is a considerable plasticity among them: different subtypes co-exist in the same tumors and shifts in subtypes can occur over time (Patel et al., 2014; Sottoriva et al., 2013). This plasticity may be explained by acquisition of new genetic and epigenetic abnormalities, by stem-like reprogramming or by clonal variation (Fedele et al., 2019). It is also not fully understood whether the distinct subtypes evolve from a common glioma precursor (Ozawa et al., 2014). For instance, PN tumors often switch phenotype to MES upon recurrence, and treatment also increases the mesenchymal gene signature, suggesting that MES transition, or epithelial to mesenchymal (EMT)-like, in GBM is associated with tumor progression and therapy resistance (Bhat et al., 2013; Halliday et al., 2014; Phillips

et al., 2006). Yet, the frequency and relevance of this EMT-like phenomenon in glioma progression remains unclear. EMT has also been associated with stemness in other cancers (Mani et al., 2008; Tam and Weinberg, 2013; Ye et al., 2015). Glioma stem cells (GSCs) share features with normal neural stem cells (NSCs) such as self-renewal and ability to differentiate into distinct cellular lineages (astrocytes, oligodendrocytes and neurons) but are thought to be the responsible for tumor relapse, given their ability to repopulate tumors and their resistance to treatment (Bao et al., 2006; Chen et al., 2012).

FOSL1, that encodes FRA-1, is an AP-1 transcription factor with prognostic value in different epithelial tumors, where its overexpression correlates with tumor progression or worse patient survival (Chiappetta et al., 2007; Gao et al., 2017; Usui et al., 2012; Vallejo et al., 2017; Wu et al., 2015; Xu et al., 2017). Moreover, the role of *FOSL1* in EMT has been documented in breast and colorectal cancers (Andreolas et al., 2008; Bakiri et al., 2015; Diesch et al., 2014; Tam et al., 2013). In GBM, it has been shown that *FOSL1* modulates *in vitro* glioma cell malignancy (Debinski and Gibo, 2005).

Here we report that *NF1* loss, by increasing RAS/MAPK activity, modulates *FOSL1* expression which in turn plays a central function in the regulation of MES GBM. Using a surrogate mouse model of MES GBM and patient-derived MES brain tumor stem cells (BTSCs), we show that *FOSL1* is responsible for sustaining cell growth *in vitro* and *in vivo*, and for the maintenance of stem-like properties. We propose that *FOSL1* is an important regulator of GBM stemness, MES features and plasticity, controlling an EMT-like process with therapeutically relevant implications.

Results

FOSL1 is a master regulator of the MES subtype

To study the tumor cell-intrinsic signaling pathways that modulate the GBM expression subtypes we assembled a collection of transcriptomic data (both expression arrays and RNA-sequencing) of 115 samples derived from 87 independent BTSC lines: 24 newly generated at Freiburg Medical Center, 44 from GSE119834 (Mack et al., 2019), 10 from GSE67089 (Mao et al., 2013) and 9 from GSE8049 (Günther et al., 2008). Samples were then classified according to the previously reported 50-gene glioma-intrinsic transcriptional subtype signatures and the single sample gene set enrichment analysis (ssGSEA)-based equivalent distribution resampling classification strategy (Wang et al., 2017). Overall, 39% of the samples were identified as CL, 41% as MES and 20% as PN (Table S1). Principal component analysis showed a large overlap of the

transcription profile among CL and PN BTSCs while most of the MES BTSCs appeared as a separate group (Figure 1A). Differential gene expression analysis comparing MES versus Non-MES (PN and CL) BTSCs confirmed a clear separation among the two groups, with the exception of a small number of cell lines that showed a mixed expression profile (Figure 1B and Table S2).

To reveal the signaling pathways underlying the differences among MES versus Non-MES BTSCs we then applied a network-based approach based on ARACNe (Algorithm for the Reconstruction of Accurate Cellular Networks) (Basso et al., 2005; Carro et al., 2010), which identifies a list of transcription factors (TFs) with their predicted targets, defined as regulons. The regulon for each TF is constituted by all the genes whose expression data exhibit significant mutual information with that of a given TF and are thus expected to be regulated by that TF (Castro et al., 2016; Fletcher et al., 2013). Enrichment of a relevant gene signature in each of the regulons can point to the TFs acting as master regulators (MRs) of the response or phenotype (Carro et al., 2010; Fletcher et al., 2013). Master regulator analysis (MRA), identified a series of TFs, among which *FOSL1*, *SOX11*, *OLIG2*, *CTCF* and *IRF1* were the top 5 most statistically significant (Benjamini-Hochberg $P < 0.0001$) (Table S3 and Figure 1C). *FOSL1* and *IRF1* were significantly upregulated in the MES BTSCs, while *SOX11*, *OLIG2*, *CTCF* were upregulated in the Non-MES BTSCs (Figure S1A and 1D). Gene set enrichment analysis (GSEA) evidenced how the regulons for the top 5 TFs are enriched for genes that are differentially expressed among the two classes (MES and Non-MES) with *FOSL1* having the highest enrichment score (Figure 1C and Figure S1B).

We then analyzed the TCGA pan-glioma dataset (Ceccarelli et al., 2016) and observed that *FOSL1* expression is elevated in the IDH-wt glioma molecular subtype (Figure 1E and Table S4) and that high expression levels are associated with worse prognosis in IDH-wt GBM (Figure 1F), thus suggesting that *FOSL1* could represent not only a master regulator of the glioma-intrinsic MES signature, but also a putative key player in MES GBM pathogenesis.

***NF1* modulates the MES signature and *FOSL1* expression**

NF1 alterations and activation of the RAS/MAPK signaling have been previously associated with the MES GBM subtype (Brennan et al., 2013; Verhaak et al., 2010; Wang et al., 2016; Wang et al., 2017). However, whether *NF1* plays a functional role in the regulation of the MES gene signature (MGS) still remains to be established.

We initially grouped, according to the previously described subtype-specific gene signatures, a subset of IDH-wt GBM samples of the TCGA dataset for which RNA-seq data were available (n = 152) (see methods for details). By analyzing the frequency of *NF1* alterations (either point mutations or biallelic gene loss) in the different subtypes (Figure 2A), we confirmed a significant enrichment of *NF1* alterations in MES versus Non-MES tumors (Fisher's Exact test P value = 0.03) (Figure 2B). Importantly, we detected higher level of *FOSL1* mRNA in the cohort of patient tumors with *NF1* alterations, both low-grade gliomas (LGGs) and GBMs (Figures 2C and Table S4), with the NF1-altered MES GBMs showing the highest expression levels (Figures 2D and Table S4).

To test whether *NF1* signaling is directly involved in the regulation of *FOSL1* and the MES subtype, we manipulated NF1 expression in patient derived tumorspheres of either the MES or PN subtype (Figure S3A-B). To recapitulate the activity of the full-length NF1 protein we transduced the cells with the NF1 GTPase-activating domain (NF1-GRD), spanning the whole predicted Ras GTPase-activating (GAP) domain (McCormick, 1990). NF1-GRD expression in the MES cell line BTSC 233 led to inhibition of RAS activity as confirmed by analysis of pERK expression upon EGF or serum stimulation (Figure S2A-B) as well as by RAS pull down assay (Figure S2C). Furthermore, analysis of a RAS-induced oncogenic signature expression by GSEA showed a strong reduction in NF1-GRD expressing cells (NES = -1.7; FDR q-value < 0.001) (Figure S2D). Most importantly, NF1-GRD expression led to a significant reduction of the MGSs (Wang signature: NES = -1.3; FDR q-value = 0.05; Phillips signature: NES = -1.7; FDR q-value < 0.001) (Figure 2E, left panels). On the contrary, Proneural gene signatures (PNGSs) were upregulated (Wang signature: NES = 1.2; FDR q-value = 0.12; Phillips signature: NES = 1.3; FDR q-value = 0.1) (Figure 2E, right panels). Western blot analysis also revealed a significant decrease of CHI3L1 expression, a well characterized mesenchymal marker, upon NF1-GRD overexpression (Figure 2F).

Mesenchymal glioblastoma cells are able to differentiate into osteocytes, a feature they share with mesenchymal stem cells (Ricci-Vitiani et al., 2008; Tso et al., 2006). Consistent with the loss of the MGS, the ability to differentiate into osteocytes was lost in the BTSC 233 MES cells transduced with the NF1-GRD, as documented by Alizarin Red staining (Figure 2G).

To further confirm whether *NF1* deletion could be sufficient to induce changes in the MGS, we then knocked down *NF1* in the NF1-expressing PN cell line BTSC 3021

(Figure 2H) and performed microarray gene expression analysis followed by GSEA. Both Wang and Phillips MGSs were enriched upon NF1 silencing (Wang: NES = 1.61; FDR q-value = 0.005; Phillips: NES = 1.9; FDR q-value < 0.001) (Figure 2I). The PNGSs instead were not significantly lost (data not shown).

Taken together, our data indicate that NF1 modulation is able to alter the MGS expression in GBM. NF1-led gene expression changes might be driven by an effect on MGS master regulators. Alternatively, other TFs might be involved. We therefore analyzed the expression of *FOSL1* and other previously described mesenchymal TFs (Bhat et al., 2011; Carro et al., 2010) upon NF1-GRD overexpression or *NF1* loss in two independent MES (BTSC 233 and BTSC 232) or PN (BTSC 3021 and BTSC 3047) cell lines. Interestingly, only *CEBPB* and *FOSL1* were consistently downregulated upon NF1-GRD expression (Figure 2J and S3C) and upregulated following *NF1* knockdown (Figures 2K and S3D). Moreover, a *FOSL1* targets signature was enriched in the *NF1* altered versus *NF1* wt GBM samples of the TCGA dataset as well as in the BTSC 3021 sh*NF1* versus shCtrl (*NF1* altered: NES = 1.38; FDR q-value = 0.16; sh*NF1*: NES = 1.9; FDR q-value < 0.001) (Figure S3E, top and middle panels). Conversely, *FOSL1* targets were downregulated upon NF1-GRD (NF1-GRD: NES = -1.38; FDR q-value = 0.037) (Figure S3E, bottom panel). These data were further confirmed by the analysis of the expression of some *FOSL1* targets (*ITGA3*, *PLAU*, *ITGA5*, *TNC* and *SERPINE1*): we observed that *ITGA3* and *SERPINE1* were consistently either downregulated upon NF1-GRD overexpression (Figure S3F, NF1-GRD in BTSC 233 and BTSC 232) or upregulated upon *NF1* knockdown (Figure S3G, sh*NF1* in BTSC 3021 and BTSC 3047).

Overall these evidences suggest that *NF1* is directly involved in the regulation of the MGS, possibly through the modulation of *FOSL1* expression.

***Fosl1* deletion induces a shift from a MES to a PN gene signature**

To further explore the *NF1-FOSL1* axis in MES GBM we used a combination of the RCAS-Tva system with the CRISPR/Cas9 technology, recently developed in our laboratory (Oldrini et al., 2018) to induce *Nf1* loss or *Kras* mutation. Mouse neural stem cells (NSCs) from *hGFAP-Tva; hGFAP-Cre; Trp53^{lox}; ROSA26-LSL-Cas9* pups were isolated and infected with viruses produced by DF1 packaging cells transduced with RCAS vectors targeting the expression of *Nf1* through shRNA and sgRNA (sh*Nf1* and sg*Nf1*) or overexpressing a mutant form of *Kras* (*Kras^{G12V}*). Loss of NF1 expression was confirmed by western blot and FRA-1 was upregulated in the two models of *Nf1* loss

compared to parental cells, and further upregulated in cells infected with *Kras*^{G12V} (Figure 3A). Consistent with activation of the Ras signaling, as result of both *Nf1* loss and *Kras* mutation, the MEK/ERK pathway was more active in infected cells compared to parental cells (Figure 3A). Higher levels of activation of the MEK/ERK pathway were associated with the induction of mesenchymal genes such as *Plau*, *Plaur*, *Timp1* and *Cd44* (Figure 3B). These data indicated that *Kras*^{G12V}–transduced cells are a suitable model to functionally study the role of *Fosl1* in MES GBM.

Taking advantage of the Cas9 expression in the generated cell p53-null *Kras*^{G12V} NSCs model, *Fosl1* expression was knocked out through sgRNAs. Efficient downregulation of FRA-1 was achieved with 2 different sgRNAs (Figure 3C). Cells transduced with sg*Fosl1*_1 and sg*Fosl1*_3 were then subjected to further studies.

As suggested by the data presented here on the human BTSCs datasets (Figures 1C-D and 2K), *FOSL1* appears to be a key regulator the MES subtype. Consistently, RNA-seq analysis followed by GSEA of p53-null *Kras*^{G12V} sg*Fosl1*_1 versus sgCtrl revealed a significant loss of Wang and Phillips MGSs (Wang: NES = -1.85; FDR q-value < 0.001; Phillips: NES = -1.91; FDR q-value < 0.001) (Figure 3D, left panels). Oppositely, Wang and Phillips PNGSs were increased in sg*Fosl1*_1 cells (Wang: NES = 1.42; FDR q-value = 0.029; Phillips: NES = 2.10; FDR q-value < 0.001) (Figure 3D, right panels). These findings were validated by qRT-PCR with a significant decrease in expression of a panel of MES genes (*Plau*, *Itga7*, *Timp1*, *Plaur*, *Fn1*, *Cyr61*, *Actn1*, *S100a4*, *Vim*, *Cd44*) (Figure 3E) and increased expression of PN genes (*Olig2*, *Ncam1*, *Bcan*, *Lgr5*) in the *Fosl1* knock-out (KO) *Kras*^{G12V} NSCs (Figure 3F).

***Fosl1* deletion reduces stemness and tumor growth**

Ras activating mutations have been widely used to study gliomagenesis, in combination with other alterations as Akt mutation (Holland et al., 2000), loss of Ink4a/Arf (Uhrbom et al., 2002) or p53 (Friedmann-Morvinski et al., 2012; Koschmann et al., 2016; Muñoz et al., 2013). Thus, we then explored the possibility that *Fosl1* could modulate the tumorigenic potential of the p53-null *Kras* mutant cells.

Cell viability was significantly decreased in *Fosl1* KO cell lines, as compared to sgCtrl (Figure 4A). Concomitantly, we observed a significant decreased percentage of cells in S-phase (mean values: sgCtrl = 42.6%; sg*Fosl1*_1 = 21.6%, P ≤ 0.001; sg*Fosl1*_3 = 20.4%, P = 0.003) and an increase in percentage of cells in G2/M (mean values: sgCtrl = 11.7%, sg*Fosl*1_1 = 28.4%, P ≤ 0.001; sg*Fosl1*_3 = 23.4%, P = 0.012) (Figure 4B).

Another aspect that contributes to GBM aggressiveness is its heterogeneity, attributable in part to the presence of glioma stem cells. By using limiting dilution assays, we found that *Fosl1* is required for the maintenance of stem cell capacity (Figure 4C). Moreover, RNA-seq analysis showed that sg*Fosl1*_1 cells downregulated the expression of stem genes (*Elf4*, *Klf4*, *Itgb1*, *Nes*, *Sall4*, *L1cam*, *Melk*, *Cd44*, *Myc*, *Fut4*, *Cxcr4*, *Prom1*) while upregulating the expression of lineage-specific genes: neuronal (*Map2*, *Ncam1*, *Tubb3*, *Slc1a2*, *Rbfox3*, *Dcx*), astrocytic (*Aldh1l1*, *Gfap*, *S100b*, *Slc1a3*) and oligodendrocytic (*Olig2*, *Sox10*, *Cnp*, *Mbp*, *Cspg4*) (Figure 4D). The different expression of some of the stem/differentiation markers was confirmed also by immunofluorescence analysis. While *Fosl1* KO cells presented low expression of the stem cell marker CD44, differentiation markers as GFAP and OLIG2 were significantly higher when compared to sgCtrl cells (Figure 4E, Figure S4).

We then sought to test whether: i) p53-null $Kras^{G12V}$ NSCs were tumorigenic and ii) *Fosl1* played any role in their tumorigenic potential. Intracranial injections of p53-null $Kras^{G12V}$ NSCs in *nu*/*nu* mice led to the development of high-grade tumors with a median survival of 37 days in control cells (n=9). However, the sg*Fosl1*_1 injected mice (n=6) had a significant increase in median survival (54.5 days, Log-rank $P = 0.0263$) (Figure 4F). Consistent with what we detected *in vitro* (Figure 3D-F) we observed a switch from a MGS to a PNGS in the tumors (Figure 4G-I). By western blot and immunohistochemical analysis, we observed a reduction on expression of MES markers (VIM, CD44 and S100A4) as compared to sgCtrl tumors (Figure 4G-H), while the PN marker OLIG2 was only found expressed in sg*Fosl1* tumors (Figure 4G). Similarly, when we compared mRNA expression of a sgCtrl tumor with high FRA-1 expression (T4, Figure 4G) with sg*Fosl1* tumors with no detectable FRA-1 expression by western blot (T3 and T4, Figure 4G), we found downregulated expression of MES markers and upregulated expression of PN markers in the sg*Fosl1* tumors (Figure 4I-J).

Altogether, our data support the conclusion that, besides controlling cell proliferation, *Fosl1* plays a critical role in the maintenance of the stem cell properties and tumorigenicity of p53-null *Kras* mutant NSCs.

Fosl1 amplifies MES gene expression

To further assess the role of *Fosl1* as a key player in the control of the MGS, we used a mouse model of inducible *Fosl1* overexpression containing the alleles $Kras^{LSLG12V}$; $Trp53^{lox}$; $ROSA26^{LSLrtTA\text{-}IRES\text{-}EGFP}$; $Col1a1^{TetO\text{-}Fosl1}$ (here referred as $Fosl1^{tetON}$). Similar to

the loss-of-function approach here used, this allelic combination allows the expression of *Kras*^{G12V} and deletion of *p53* after Cre recombination. Moreover, the expression of the reverse tetracycline transactivator (rtTA) allows, upon induction with doxycycline (Dox), the ectopic expression of *Fosl1* (Flag tagged), under the control of the *Col1a1* locus and a tetracycline-responsive element (TRE or Tet-O) (Belteki et al., 2005; Hasenfuss et al., 2014).

NSCs derived from *Fosl1*^{WT} and *Fosl1*^{tetON} mice were infected *in vitro* with a lentiviral vector expressing the Cre recombinase and efficient infection was confirmed by fluorescence microscopy, as the cells expressing the rtTA should express GFP (data not shown). FRA-1 overexpression, as well as Flag-tag expression was then tested by western blot after 72h of Dox induction (Figure 5A). When *Fosl1*^{tetON} NSCs were analyzed by qRT-PCR for the expression of MES/PN markers, a significant upregulation of most MES genes and downregulation of PN genes was found in the cells overexpressing *Fosl1* upon Dox induction (Figure 5B-C), the inverse image of our findings with *Fosl1* knock-out cells.

In order to investigate if the MES phenotype induced with *Fosl1* overexpression would have any effect *in vivo*, p53-null *Kras*^{G12V} *Fosl1*^{tetON} NSCs were intracranially injected into syngeneic C57BL/6J wildtype mice. Injected mice were randomized and subjected to Dox diet (food pellets and drinking water) or kept as controls with regular food and drinking water with 1% sucrose. No differences in mice survival were observed (Figure S5B). However, tumors developed from *Fosl1* overexpressing mice (+Dox) were larger (Figure 5D), more infiltrative and with a more aggressive appearance than controls (–Dox), that mostly grew as superficial tumor masses, even if both –Dox and +Dox tumors seem to proliferate similarly (Figure S5C).

Tumorspheres were derived from –Dox and +Dox tumor-bearing mice and *Fosl1* expression was manipulated *in vitro* through addition or withdrawal of Dox from the culture medium. In the case of tumorspheres derived from a –Dox tumor, when Dox was added for 19 days, high levels of FRA-1 expression were detected by western blot (Figure 5E). At the mRNA level, Dox treatment also greatly increased *Fosl1* expression, as well as some of the MES genes (Figure 5F), while the expression of PN genes was downregulated (Figure 5G). Conversely, when Dox was removed from +Dox derived tumorspheres for 19 days, the expression of FRA-1 decreased (Figure 5H-I), along with the expression of MES genes (Figure 5I), while PN genes were upregulated (Figure 5J). These results confirm the essential role of *Fosl1* in the regulation of the MES gene

signature in p53-null *Kras*^{G12V} tumor cells and the plasticity between the PN and MES subtypes.

FOSL1 controls growth, stemness and MES gene expression in patient-derived tumor cells

To prove the relevance of our findings in the context of human tumors, we analyzed BTSC lines characterized as Non-MES (BTSC 268 and 409) or MES (BTSC 349 and 380) (Figure 1A). By western blot, we found that MES BTSC 380 did not express NF1 while BTSC 349 showed a different pattern of NF1 expression compared to the Non-MES lines BTSC 268 and 409 (intact NF1), that might be due to a *NF1* point mutation. Consistent with the observed upon *NF1* silencing either in human BTSCs (Figure 2I) or mouse NSCs (Figure 3A), both MES cell lines expressed high levels of FRA-1 and activation of the MEK/ERK pathway (Figure 6A).

To study the role of *FOSL1* in the context of human BTSCs, its expression was silenced in the MES BTSC 349, the cell line with higher FRA-1 expression, using a Dox inducible shRNA. We confirmed by western blot FRA-1 downregulation after 3 days of Dox treatment (Figure 6B). Similar to what was observed in the mouse cells, *FOSL1* silencing in MES BTSC 349 resulted in reduced cell growth (Figure 6C) with a significant reduction of the percentage of BrdU positive cells, compared to Dox-untreated cells (Figure S6A). *FOSL1* silencing through Dox treatment also decreased stem cell sphere forming capacity of MES BTSC 349 (Figure 6D). Moreover, *FOSL1* silencing resulted also in the significant downregulation of the MES genes (Figure 6E), while no major differences in the expression of PN genes was observed (Figure S6B).

Lastly, we tested whether FRA-1 modulates the MGS via direct target regulation. To this end, we first identified high-confidence *FOSL1*/FRA-1 binding sites in chromatin immunoprecipitation-seq (ChIP-seq) generated in non-mesenchymal cancer cells (see methods) and then we determined the counts per million reads (CPM) of the enhancer histone mark H3K27Ac in a set of MES and non-MES BTSCs (Mack et al., 2019). Differential enrichment analysis by DeSeq2 revealed 9262 regions statistically significant for H3K27Ac at *FOSL1*/FRA-1 binding sites in either MES or non-MES BTSCs (Figure 6F). Gene set enrichment analysis revealed that a significant fraction of H3K27Ac-decorated *FOSL1*/FRA-1 binding sites was enriched in MES BTSCs and PCA further revealed that H3K27Ac-decorated sites in MES BTSCs clustered closer to *FOSL1*/FRA-1 direct binding to chromatin when compared to non-MES BTSCs (Figure 6G). Next, we

compared H3K27Ac distribution over *FOSL1*/FRA-1 binding sites to that of the Non-MES master regulator OLIG2 (Figure 1C). This analysis showed that the 9262 *FOSL1*/FRA-1 binding sites are systematically decorated with H3K27Ac in MES BTSCs, whereas only 3423 out of 9262 sites are acetylated to a similar extent in non-MES BTSCs. Importantly, the inverse trend was observed for H3K27Ac at OLIG2 binding sites (Figure 6H). Validation in an independent MES BTSC line (BTSC 349) by ChIP-qPCR confirmed FRA-1 binding at promoters of some MES genes including *PLAU*, *TNC*, *ITGA5* and *CD44* (Figure 6J).

Altogether, our data support that *FOSL1*/FRA-1 regulates MES gene expression and aggressiveness in human gliomas via direct transcriptional regulation, downstream of NF1.

Discussion

The most broadly accepted transcriptional classification of GBM was originally based on gene expression profiles of bulk tumors (Verhaak et al., 2010), which did not discriminate the contribution of tumor cells and TME to the transcriptional signatures. It is now becoming evident that both cell-intrinsic and extrinsic cues can contribute to the specification of the MES subtype (Bhat et al., 2013; Neftel et al., 2019; Wang et al., 2017). Bhat and colleagues had shown that while some of the MES GBMs maintained the mesenchymal characteristics when expanded *in vitro* as BTSCs, some others lost the MGS after few passages while exhibiting a higher PNGS (Bhat et al., 2013). These data, together with the evidence that xenografts into immunocompromised mice of BTSCs derived from MES GBMs were also unable to fully restore the MES phenotype, suggested that the presence of an intact TME potentially contributed to the maintenance of a MGS, either by directly influencing a cell-intrinsic MGS or by expression of the TME-specific signature. Recently, the transcriptional GBM subtypes were redefined based on the expression of glioma-intrinsic genes, thus excluding the genes expressed by cells of the TME (Wang et al., 2017). Our master regulator analysis on the BTSCs points to the AP-1 family member *FOSL1* as one of the top transcription factors contributing to the cell-intrinsic MGS. Previous tumor bulk analysis identified a related AP-1 family member *FOSL2*, together with *CEBPB*, *STAT3* and *TAZ*, as important regulators of the MES GBM subtype (Bhat et al., 2011; Carro et al., 2010). While *FOSL1* was also listed as a putative MES master regulator (Carro et al., 2010), its function and mechanism of action have not been further characterized since then. Our experimental data show that *FOSL1* is a key

391 regulator of GBM subtype plasticity and MES transition, and define the molecular
392 mechanism through which *FOSL1* is regulated.

393 Although consistently defined, GBM subtypes do not represent static entities. The
394 plasticity between subtypes happens at several levels. Besides the referred MES-to-PN
395 change in cultured GSCs compared to the parental tumor (Bhat et al., 2013), a PN-to-
396 MES shift often occurs upon treatment and recurrence. Several independent studies
397 comparing matched pairs of primary and recurrent tumors demonstrated a tendency to
398 shift towards a MES phenotype, associated with a worse patient survival, likely as a result
399 of treatment-induced changes in the tumor and/or the microenvironment (Phillips et al.,
400 2006; Wang et al., 2016; Wang et al., 2017). Moreover, distinct subtypes/cellular states,
401 can coexist within the same tumor (Neftel et al., 2019; Patel et al., 2014; Sottoriva et al.,
402 2013; Wang et al., 2019) and targeting these multiple cellular components could result in
403 more effective treatments (Wang et al., 2019).

404 PN-to-MES transition is often considered an EMT-like phenomenon, associated
405 with tumor progression (Fedele et al., 2019). The role of *FOSL1* in EMT has been studied
406 in other tumor types. In breast cancer cells *FOSL1* expression correlates with
407 mesenchymal features and drives cancer stem cells (Tam et al., 2013) and the regulation
408 of EMT seems to happen through the direct binding of FRA-1 to promoters of EMT genes
409 such as Tgfb1, Zeb1 and Zeb2 (Bakiri et al., 2015). In colorectal cancer cells, *FOSL1* was
410 also shown to promote cancer aggressiveness through EMT by direct transcription
411 regulation of EMT-related genes (Diesch et al., 2014; Liu et al., 2015).

412 It is well established that *NF1* inactivation is a major genetic event associated with
413 the MES subtype (Verhaak et al., 2010; Wang et al., 2017). However, this is probably a
414 late event in MES gliomagenesis, as all tumors possibly arise from a PN precursor and
415 just later in disease progression acquire *NF1* alterations that are directly associated with
416 a transition to a MES subtype (Ozawa et al., 2014). Moreover, *NF1* deficiency has been
417 recently linked to macrophage/microglia infiltration in the MES subtype (Wang et al.,
418 2017). The fact that the enriched macrophage/microglia microenvironment is also able to
419 modulate a MES phenotype suggests that there might be a two-way interaction between
420 tumor cells and TME. The mechanisms of NF1-regulated chemotaxis and whether this
421 relationship between the TME and MGS in GBM is causal remain elusive.

422 Here we provide evidence that manipulation of *NF1* expression levels in patient-
423 derived BTSCs has a direct consequence on the tumor-intrinsic MGS activation and that
424 such activation, can at least in part be mediated by the modulation of *FOSL1*. Among the

previously validated MRs, only *CEBPB* appears also to be finely modulated by *NF1* inactivation. This suggests that among the TFs previously characterized (such as *FOSL2*, *STAT3*, *BHLHB2* and *RUNX1*), *FOSL1* and *CEBPB* might play a specific role in the *NF1*-mediated MES transition that occurs in glioma cells with limited or possibly absent effect by the TME. However, whether *FOSL1* contributes also to the putative cross-talk between the TME and the cell-intrinsic MGS, will still have to be established.

Furthermore we show that *FOSL1* is a crucial player in glioma pathogenesis, particularly in a MAPK-driven MES GBM context. Our findings broaden its previously described role in KRAS-driven epithelial tumors, such as lung and pancreatic ductal adenocarcinoma (Vallejo et al., 2017). *NF1* inactivation results in Ras activation, which stimulates downstream pathways as MAPK and PI3K/Akt /mTOR. RAS/MEK/ERK activation in turn regulates *FOSL1* mRNA expression and FRA-1 protein stability (Casalino et al., 2003; Verde et al., 2007). FRA-1 can then directly bind and activate some of the MES genes, while possibly binding its own promoter to activate its own expression (Diesch et al., 2014; Lau et al., 2016). This generates a feedback loop that induces MGS, increases proliferation and stemness, sustaining tumor growth. FRA-1 requires, for its transcriptional activity, heterodimerization with the AP-1 transcription factors JUN, JUNB or JUND (Eferl and Wagner, 2003). Which of the JUN family members participate in the MES gene regulation and whether FRA-1 activates MES gene expression and simultaneously represses PN genes, requires further investigation.

In conclusion, *FOSL1* is a master regulator of the MES subtype of GBM, significantly contributing to its stem cell features, which could open new therapeutic options. Although *FOSL1* pharmacological inhibition is difficult to achieve due to the lack of specific inhibitors, a gene therapy approach targeting *FOSL1* expression through CRISPR, for instance, could constitute an attractive alternative to treat MES GBM patients.

Acknowledgements

We would like to thank Álvaro Ucero for his input on the project and Flora A. Díaz for her technical support. We are grateful to Francisco X. Real and Scott Lowe for critical input on the manuscript. We thank Pamela Franco for experimental support and discussion. This work was supported by a grant from the Marie Curie International re-integration Grants (MC-IRG), project nr. 268303 (to M.S.C.) and by grants from the

ISCIII, project PI13/01028, cofounded by the European Regional Development Fund (ERDF), and from the Seve Ballesteros Foundation (to M.S.).

Author Contributions

C.M designed and performed experiments, analyzed data and wrote the manuscript. T.U., P.K., A.I. and E.K. performed experiments. G.G. analyzed data and interpreted experiments. O.S. provided tumor samples. S.N. provided cell lines. L.B. and E.F.W. provided reagents, contributed to experimental design and interpreted experiments. M.S.C and M.S. conceived the project, designed and interpreted experiments and wrote the manuscript.

Declaration of interests

The authors declare no competing interests.

Material and Methods

Generation of the BTSCs dataset and Master regulator analysis (MRA)

The brain tumor stem cell lines (BTSCs) dataset was assembled with new and previously generated transcriptomic data: 24 Illumina HumanHT-12v4 expression BeadChip microarrays newly generated at Freiburg University (GSE137310, this study); 44 RNA-seq samples (Illumina HiSeq 2500) from GSE119834 (Mack et al., 2019), 30 Affymetrix Human Genome U219 microarrays from GSE67089 (Mao et al., 2013) and 17 Affymetrix HG-U133 Plus 2.0 microarrays from GSE8049 (Günther et al., 2008). For the previously published data, at exception of the GSE119834, for which pre-processed data were used, raw data were downloaded from the GEO repository (https://www.ncbi.nlm.nih.gov/geo/) and subsequently the 'affy' package (R programming language) was used for robust multi-array average normalization followed by quantile normalization. For genes with several probe sets, the median of all probes had been chosen and only common genes among all the datasets (n = 14821) were used for further analysis. To avoid issues with the use of different transcriptomic platforms each dataset was then scaled (mean = 0, sd = 1) before assembling the combined final dataset. Transcriptional subtypes were obtained using the 'ssgsea.GBM.classification' R package (Wang et al., 2017), through the SubtypeME tool of the GlioVis web portal

(http://gliovis.bioinfo.cnio.es) (Bowman et al., 2017). Differential gene expression (MES vs Non-MES BTSCs) was performed using the 'limma' R package.

The master regulator analysis was performed using the 'RTN' R package (Castro et al., 2016). Normalized BTSC expression data were used as input to build a transcriptional network (TN) for 785 TFs present in the dataset. TF annotations were obtained from Gene Ontology (GO:0003700). P values for network edges were computed from a pooled null distribution using 1000 permutations. Edges with an adjusted-P value < 0.05 were kept for data processing inequality (DPI) filtering. In the TN, each target can be connected to multiple TFs and regulation can occur as a result of both direct and indirect interactions. DPI-filtering removes the weakest interaction in any triangle of two TFs and a target gene, therefore preserving the dominant TF-target pairs and resulting in a filtered TN that highlights the most significant interactions (Fletcher et al., 2013). Post-DPI filtering, the MRA computes the overlap between the transcriptional regulatory unities (regulons) and the input signature genes using the hypergeometric distribution (with multiple hypothesis testing corrections). To identify master regulators, the differential gene expression between MES and Non-MES was used as a phenotype.

TCGA pan-glioma data analysis

RSEM normalized RNA-seq data for the TCGA GBMLGG dataset were downloaded from the Broad Institute Firebrowse (http://gdac.broadinstitute.org). *NF1* copy number alterations and point mutations were obtained at the cBioPortal (https://www.cbioportal.org). Transcriptional subtypes were inferred using the 'ssgsea.GBM.classification' R package as indicated above. Glioma molecular subtypes information was downloaded from the GlioVis web portal (http://gliovis.bioinfo.cnio.es) (Bowman et al., 2017). Survival analysis was performed using the 'survival' R package.

Gene Expression Array and gene set enrichment analysis (GSEA)

For gene expression profiling of the BTSC lines of the Freiburg dataset, total RNA was prepared using the RNeasy kit (Qiagen #74104) or the AllPrep DNA/RNA/Protein mini kit (Qiagen #80004) and quantified using 2100 Bioanalyzer (Agilent). One-and-a-half µg of total RNA for each sample was sent to the genomic facility of the German Cancer Research Center (DKFZ) in Heidelberg (Germany) where hybridization and data normalization were performed. Hybridization was carried out on Illumina HumanHT-

12v4 expression BeadChip. Gene set enrichment analysis was performed using the GSEA software (http://www.broadinstitute.org/gsea/index.jsp).

ChIP-seq analysis

We downloaded FOSL1 ChIP-seq profiling from ENCODE tracks ENCFF000OZR and ENCFF000OZQ. OLIG2 binding sites and ChIP-seq profiles were downloaded from GEO: GSM1306365_MGG8TPC.OLIG2r1c and GSM1306367_MGG8TPC.OLIG2r2. H3K27Ac data were downloaded from GSE119755 (Mack et al., 2019) for GSM3382291_GSC17, GSM3382343_GSC40, GSM3382319_GSC3, GSM3382321_GSC30, GSM3382341_GSC4, GSM3382277_GSC10. Scatter plots were generated with Seqmonk v1.45 using FOSL1 binding sites in MES-BTSCs using a Kolmorogov-Smirnov test with a sample size of 297 when constructing the control distributions and filtering by maximum P value of 0.05 (multiple testing correction applied). Minimum absolute z-score was 0.5. A custom regression was calculated. Quantitation was Read Count Quantitation using all reads correcting for total count only in probes to largest store log transformed duplicates ignored. Heatmaps were generated using ChaSE, using either FOSL1 or OLIG2 binding sites with ±10,000 bp.

Mouse strains and husbandry

GFAP-tv-a; hGFAP-Cre; Rosa26-LSL-Cas9 mice were previously described (Oldrini et al., 2018). $Kras^{LSLG12V}$; $Trp53^{lox}$; $Rosa26^{LSLrtTA\text{-}IRES\text{-}EGFP}$; $Col1a1^{TetO\text{-}Fosl1}$ mouse strain corresponds to the MGI Allele References 3582830, 1931011, 3583817 and 5585716, respectively. Immunodeficient *nu*/*nu* mice (MGI: 1856108) were obtained at the Spanish National Cancer Research Centre Animal Facility.

Mice were housed in the specific pathogen-free animal house of the Spanish National Cancer Research Centre under conditions in accordance with the recommendations of the Federation of European Laboratory Animal Science Associations (FELASA). All animal experiments were approved by the Ethical Committee (CEIyBA) and performed in accordance with the guidelines stated in the International Guiding Principles for Biomedical Research Involving Animals, developed by the Council for International Organizations of Medical Sciences (CIOMS).

Cell lines and cell culture

Mouse neural stem cells (NSCs) were derived from the whole brain of newborn mice of *Gtv-a; hGFAP-Cre; LSL-Cas9; Trp53*^{lox} (referred as p53-null NSCs) and *Kras*^{LSLG12V}*; Trp53*^{lox}*; Rosa26*$^{LSLrtTA\text{-}IRES\text{-}EGFP}$*; Col1a1*$^{TetO\text{-}Fosl1}$ (referred as *Fosl1*^{TetON} NSCs). Tumorsphere lines were derived from tumors of C57BL/6J injected with *Fosl1*^{TetON} NSCs, when mice were sacrificed after showing symptoms of brain tumor disease. For the derivation of mouse NSCs and tumorspheres, tissue was enzymatically digested with 5 mL of papain digestion solution (0.94 mg/mL papain (Worthington #LS003119), 0.48 mM EDTA, 0.18 mg/mL N-acetyl-L-cysteine (Sigma-Aldrich #A9165) in Earl's Balanced Salt Solution (Gibco #14155-08)) and incubated at 37°C for 8 min. After digestion, the enzyme was inactivated by the addition of 2 mL of 0.71 mg/mL ovomucoid (Worthington #LS003087) and 0.06 mg/mL DNaseI (Roche #10104159001) diluted in Mouse NeuroCult basal medium (Stem Cell Technologies #05700) without growth factors. Cell suspension was centrifuged at a low speed and then passed through a 40 µm mesh filter to remove undigested tissue, washed first with PBS and then with ACK lysing buffer (Gibco #A1049201) to remove red blood cells. NSCs and tumorspheres were grown in Mouse NeuroCult basal medium, supplemented with Proliferation supplement (Stem Cell Technologies #05701), 20 ng/mL recombinant human EGF (Gibco #PHG0313), 10 ng/mL basic-FGF (Millipore #GF003-AF), 2 µg/mL Heparin (Stem Cell Technologies #07980) and L-glutamine (2mM, Hyclone #SH3003401). Spheres were dissociated with Accumax (ThermoFisher Scientific #00-4666-56) and re-plated every 4-5 days.

Patient-derived glioblastoma stem cells (BTSCs) were prepared from tumor specimens under IRB-approved guidelines as described before (Fedele et al., 2017). BTSCs were grown as neurospheres in Neurobasal medium (Gibco #10888022) containing B27 supplement (Gibco #12587010), N2 supplement (Gibco #17502048), b-FGF (20 ng/mL), EGF (20 ng/mL), LIF (10 ng/mL, CellGS #GFH200-20), 2 µg/mL Heparin and L-glutamine (2mM). JX6 were kindly provided by Y. Gillespie (UAB, Birmingham).

Vectors, virus production and infection

Flag-tagged NF1-GRD (aminoacids 1131-1534) was amplified by PCR from human cortical tissue (epilepsy patient) and first cloned in the pDRIVE vector. Primers are listed in Table S5. The NF1-GRD sequence was then excised by restriction digestion using PmeI and SpeI enzymes and subcloned in the modified pCHMWS lentiviral vector

(kind gift from V. Baekelandt, University of Leuven, Belgium) sites by removing the fLUC region. The correct sequence was verified by sequencing. For *NF1* silencing, *NF1* short hairpin from pLKO (Sigma, TRCN0000238778) vector was subcloned in pGIPZ lentiviral vector (Open Biosystems). The corresponding short hairpin sequence was synthetized (GATC) and amplified by PCR using XhoI and EcoRI sites containing primers. The PCR product was digested using XhoI and EcoRI and subcloned into the pGIPZ vector previously digested with XhoI and PmeI following by digestion with EcoRI. The two vector fragments were ligated with *NF1* short hairpin fragment. The correct insertion and sequence was validated by sequencing. In addition, experiments were performed using sh*NF1*-pGIPZ clone V2LHS_76027 (clone 4) and V2LHS_260806 (clone 5).

RCAS viruses (RCAS-sh*Nf1*, RCAS-sg*Nf1* and RCAS-*Kras*^{G12V}) used for infection of p53-null NSCs were obtained from previously transfected DF1 chicken fibroblasts (ATCC #CRL-12203) using FuGENE 6 Transfection reagent (Promega #E2691), according to manufacturer's protocol. DF1 cells were grown at 39°C in DMEM containing GlutaMAX™ (Gibco #31966-021) and 10% FBS (Sigma-Aldrich #F7524).

The pKLV-U6gRNA-PGKpuro2ABFP was a gift from Dr. Kosuke Yusa (Wellcome Sanger Insitute) (Addgene plasmid #50946). For cloning of single gRNAs, oligonucleotides containing the BbsI site and the specific gRNA sequences were annealed, phosphorylated and ligated into the pKLV-U6gRNA(BbsI)-PGKpuro2ABFP previously digested with BbsI. Single gRNAs to target *Fosl1* were designed with Guide Scan (http://www.guidescan.com/) and the sequences cloned were sg*Fosl1*_1: TACCGAGACTACGGGGAACC; sg*Fosl1*_2: CCTAGGGCTCGTATGACTCC; sg*Fosl1*_3: ACCGTACGGGCTGCCAGCCC. These vectors and a non-targeting sgRNA control were used to transduce p53-null *Kras*^{G12V} NSCs.

The pLVX-Cre and respective control vector were kindly provided by Dr. Maria Blasco (CNIO) and used to transduce *Fosl1*^{TetON} NSCs; pLKO.1-TET-sh*FOSL1* and respective control vector were a gift from Dr. Silve Vicent (CIMA, Navarra University).

Gp2-293 packaging cell line (Clontech #631458) was grown in DMEM (Sigma-Aldrich #D5796) with 10% FBS. Lentiviruses generated in this cell line were produced using calcium-phosphate precipitate transfection and co-transfected with second-generation packaging vectors (pMD2G and psPAX2). High-titer virus was collected at 36 and 60 h following transfection.

All cells were infected with lenti- or retroviruses by four cycles of spin infection (200 × g for 2 h), in presence of 8 µg/mL polybrene (Sigma-Aldrich #H9268). Transduced cells were selected after 48 h from the last infection with 1 µg/mL Puromycin (Sigma-Aldrich #P8833).

Generation of murine gliomas

p53-null *Kras*^{G12V} NSCs (5×10^5 cells) were injected intracranially into 4 to 5 weeks-old immunodeficient *nu*/*nu* mice.

Fosl1^{TetON} NSCs (5×10^5 cells) were intracranially injected into 4 to 5 weeks-old wildtype C57Bl/6J mice that were fed *ad libitum* with 2 g/kg doxycycline-containing pellets. Due to the limited penetration of the blood brain barrier and to insure enough Dox was reaching the brain, 2 mg/mL Dox (PanReac AppliChem #A29510025) was also added to drinking water with 1% sucrose (Sigma-Aldrich #S0389) (Annibali et al., 2014; Mansuy and Bujard, 2000). Control mice were kept with regular food and 1% sucrose drinking water.

Mice were anaesthetized with 4% isofluorane and then injected with a stereotactic apparatus (Stoelting) as previously described (Hambardzumyan et al., 2009). After intracranial injection, all mice were routinely checked and sacrificed when developed symptoms of disease (lethargy, poor grooming, weight loss and macrocephaly).

Immunohistochemistry

Tissue samples were fixed in 10% formalin, paraffin-embedded and cut in 3 µm sections, which were mounted in Superfrost Plus microscope slides (Thermo Scientific #J1810AMNZ) and dried. Tissues were deparaffinized in xylene and re-hydrated through graded concentrations of ethanol in water, ending in a final rinse in water.

For histopathological analysis, sections were stained with hematoxylin and eosin (H&E).

For immunohistochemistry, deparaffinized sections underwent heat-induced antigen retrieval, endogenous peroxidase activity was blocked with 3% hydrogen peroxide (Sigma-Aldrich #H1009) for 15 min and slides were then incubated in blocking solution (2.5% BSA (Sigma-Aldrich #A7906) and 10% Goat serum (Sigma-Aldrich #G9023), diluted in PBS) for at least 1 h. Incubations with anti-FRA-1 (Santa Cruz #sc-183, 1:100) and anti-CD44 (BD Biosciences #550538, 1:100) were carried out overnight at 4°C. Slides were then incubated with secondary anti-rabbit (Vector #BA-1000) or anti-

rat (Vector #BA-9400) for 1 h at RT and with AB (avidin and biotinylated peroxidase) solution (Vectastain Elite ABC HRP Kit, Vector, PK-6100) for 30 min. Slides were developed by incubation with peroxidase substrate DAB (Vector SK-4100) until desired stain intensity. Finally, slides were counterstained with hematoxylin, cleared and mounted with a permanent mounting medium.

Immunohistochemistry for S100A4 (Abcam #ab27957, 1:300) and Ki67 (Master Diagnostica #0003110QD, undiluted) was performed using an automated immunostaining platform (Ventana discovery XT, Roche).

Immunoblotting

Cell pellets or frozen tumor tissues were lysed with JS lysis buffer (50 mM HEPES, 150 mM NaCl, 1% Glycerol, 1% Triton X-100, 1.5 mM MgCl2, 5 mM EGTA) and protein concentrations were determined by DC protein assay kit II (Bio-Rad #5000112). Proteins were separated on house-made SDS-PAGE gels and transferred to nitrocellulose membranes (Amersham #10600003). Membranes were incubated in blocking buffer (5% milk in TBST) and then with primary antibody overnight at 4°C. The following primary antibodies and respective dilutions were used: FLAG (Cell Signaling Technology #2368S, 1:2000), FRA-1 (Santa Cruz #sc-183, 1:1000; #sc-605, 1:1000), GFAP (Sigma-Aldrich #G3893, 1:5000), NF1 (Santa Cruz #sc-67, 1:500; Bethyl #A300-140A, 1:1000), OLIG2 (Millipore #AB9610, 1:2000), VIMENTIN (Cell Signaling Technology #5741, 1:3000), p-ERK1/2 (T202/Y204) (Cell Signaling Technology, #9101, 1:2000/3000; Assay Designs #ADI-905-651, 1:250), ERK1/2 (Cell Signaling Technology, #9102, 1:1000; Abcam #ab17942, 1:1000), p-MEK (S217/221) (Cell Signaling Technology, #9154, 1:500/1000), MEK (Cell Signaling Technology, #9122 1:1000), CHI3L1 (Qidel #4815, 1:1000), p85 (Millipore #06-195, 1:10000), VINCULIN (Sigma-Aldrich #V9131, 1:10000) and α-TUBULIN (Abcam #ab7291, 1:10000). Anti-mouse or rabbit-HRP-conjugated antibodies (Jackson ImmunoResearch, #115-035-003 and #111-035-003) were used to detect desired protein by chemiluminescence with ECL Detection Reagent (Amersham, #RPN2106).

Reverse transcription quantitative PCR

RNA from NSCs and frozen tissue was isolated with TRIzol reagent (Invitrogen #15596-026) according to the manufacturer's instructions. For reverse transcription PCR (RT-PCR), 500 ng of total RNA was reverse transcribed using the High Capacity cDNA

Reverse Transcription Kit (Applied Biosystems #4368814). Quantitative PCR was performed using the SYBR Select Master Mix (Applied Biosystems #4472908) according to the manufacturer's instructions. qPCRs were run and the melting curves of the amplified products were used to determine the specificity of the amplification. The threshold cycle number for the genes analyzed was normalized to GAPDH. Mouse and human primer sequences are listed in Table S5.

RNA from BTSC cells was prepared using the RNeasy kit or the AllPrep DNA/RNA Protein Mini Kit and used for first strand cDNA synthesis using random primers and SuperscriptIII reverse transcriptase (Life Technologies #18080-085). Primer sequences used in qRT-PCR with SYBR Green are listed in Table S5. Quantitative real-time PCR (qRT-PCR) STAT3 and CEBPB were performed using pre-validated TaqMan assays (Applied Biosystems): STAT3: Hs01047580, CEBPB: Hs00270923 and 18s rRNA: Hs99999901.

MTT assay

Cells were seeded in 96-well culture plates (1000 cells per well, 10 wells per cell line) and grown for 7 days. At each timepoint (days 1, 3, 5 and 7), cell viability was determined by MTT assay. Briefly, 10 µL of 5 mg/mL MTT (Sigma-Aldrich #M5655) was added to each well and cells were incubated for 4 h before lysing with a formazan solubilization solution (10% SDS in 0.01 M HCl). Colorimetric intensity was quantified using a plate reader at 590 nm. Values were obtained after subtraction of matched blanks (medium only).

Cell cycle analysis: Propidium iodide (PI) staining

Cells were harvested and washed twice with PBS prior to fixation with 70% cold ethanol, added drop-wise to the cell pellet while vortexing. Fixed cells were then washed, first with 1% BSA in PBS, then with PBS only and stained overnight with 50 µg/mL PI (Sigma-Aldrich #P4170) and 100 µg/mL RNase A (Roche #10109142001) in PBS. Samples were acquired in a FACSCanto II cytometer (BD Biosciences) and data were analyzed using FlowJo software.

BrdU incorporation

Cells were pulse-labelled with 10 µM BrdU (Sigma-Aldrich #B9285) for 2 h, harvested and washed twice with PBS prior to fixation with 70% ethanol cold ethanol,

added drop-wise to the cell pellet while vortexing. DNA denaturation was performed by incubating samples for 10 min on ice with 0.1 M HCl with 0.5% Tween-20 and samples were then resuspended in water and boiled at 100°C for 10 min. Anti-BrdU-FITC antibody (BD Biosciences #556028) was incubated according to manufacturer's protocol. After washing with PBSTB (PBS with 0.5% Tween-20 and 1% BSA), samples were resuspended in 25 µg/mL PI and 100 µg/mL RNase A diluted in PBS. Samples were acquired in a FACSCanto II cytometer (BD Biosciences) and data were analyzed using FlowJo software.

Immunofluorescence

Cells were plated in laminin-coated coverslips and fixed with 4% PFA for 15 min. Cells were then permeabilized with 0.1% Triton X-100 in 0.2% BSA and coverslips were washed and blocked with 10% donkey serum in 0.2% BSA for 1 h. The following primary antibodies were incubated overnight at 4°C: CD44 (BD Biosciences #550538, 1:100), GFAP (Millipore #MAB360, 1:400) and OLIG2 (Millipore #AB9610, 1:100). Secondary antibodies at 1:400 dilution (from Invitrogen, Alexa-Fluor anti-rabbit-488, anti-mouse-488 and anti-rat 594) were incubated for 1 h at RT and after washing coverslips were incubated for 4 min with DAPI (1:4000, Sigma-Aldrich #D8417) and mounted with ProLong Gold Antifade reagent (Invitrogen #P10144).

Fluorescence signal was quantified as the ratio of green/red pixel area relative to DAPI pixel area per field of view, in a total of 36 fields per condition analyzed.

Neurosphere formation assay and limiting dilution analysis

Neurospheres were dissociated and passed through a 40 µm mesh filter to eliminate non-single cells. Decreasing cell densities were plated in ultra-low attachment 96-well plates (Corning #CLS3474) and fresh medium was added every 3-4 days. The number of positive wells for presence of spheres was counted 2 weeks after plating. Limiting dilution analysis was performed using ELDA R package (http://bioinf.wehi.edu.au/software/elda/).

RNA-sequencing and analysis on mouse NSCs

One microgram of total RNA from the samples was used. cDNA libraries were prepared using the "QuantSeq 3‘ mRNA-Seq Library Prep Kit (FWD) for Illumina" (Lexogen #015) by following manufacturer instructions. Library generation is initiated

by reverse transcription with oligo(dT) priming, and a second strand synthesis is performed from random primers by a DNA polymerase. Primers from both steps contain Illumina-compatible sequences. Adapter-ligated libraries were completed by PCR, applied to an Illumina flow cell for cluster generation and sequenced on an Illumina HiSeq 2500 by following manufacturer's protocols. Sequencing read alignment and quantification and differential gene expression analysis was performed in the Bluebee Genomics Platform, a cloud-based service provider (www.bluebee.com). Briefly, reads were first trimmed with bbduk from BBTools (BBMap – Bushnell B, https://sourceforge.net/projects/bbmap/) to remove adapter sequences and polyA tails. Trimmed reads were aligned to the GRCm38/mm10 genome assembly with STAR v 2.5 (Dobin et al., 2013). Read counting was performed with HTSeq (Anders et al., 2015). Differential gene expression analysis was performed with DESeq2 (Love et al., 2014). The list of stem/differentiation markers was compiled by combining a previously described gene list (Sandberg *et al.* 2013) with other markers (Bazzoli et al., 2012). GSEAPreranked (Subramanian et al., 2005) was used to perform gene set enrichment analysis of the described indicated signatures on a pre-ranked gene list, setting 1000 gene set permutations.

Osteogenesis Differentiation Assay

The osteogenesis differentiation assay was performed using the StemPro Osteogenesis Differentiation Kit (Life Technologies #A1007201) according to the manufacturer's instructions. Briefly, 5×10^3 cells/cm^2 were seeded on laminin-coated glass coverslips in a 24-well cell culture plate. Cells were incubated in MSC Growth Medium at 37°C, 5% CO_2 for 21 days, replacing the medium every 4 days. Cells were then fixed with 4% formaldehyde, stained with Alizarin Red S solution (pH 4.2) and mounted on microscope slides. Pictures were acquired using an Axiovert Microscope (Zeiss).

Active Ras pull down assay

Active Ras pull down assay was performed using Active Ras pull down assay kit (ThermoFisher Scientific #16117) according to the manufacturer's instructions. Briefly, cells were grown in 10 cm plates at 80-90% confluency in presence or absence of growth factors (EGF, FGF and LIF), and lysed with the provided buffer. Lysates were incubated

with either GDP or GTP for 30 min followed by precipitation with GST-Raf1-RBD. Western blot was performed with the provided anti-RAS antibody (1:250).

Chromatin preparation and FRA-1 ChIP

BTSC cells were collected at 2×10^6 cells confluency, washed in PBS and fixed by addition of 1% formaldehyde for 20 min at room temperature. The cells were resuspended in 2 mL Lysis Buffer (50 mM Tris pH 7.5; 1 mM EDTA pH 8.0; 1% Triton; 0.1% Na-deoxycholate; 150 mM NaCl; protease inhibitors) on ice for 20 min. The suspension was sonicated in a cooled Bioruptor Pico (Diagenode), and cleared by centrifugation for 10 min at 13000 rpm. The chromatin (DNA) concentration was quantified using NanoDrop (Thermo Scientific) and the sonication efficiency monitored on an agarose gel. Protein A/G plus-agarose beads (Santa Cruz #sc-2003) were blocked with sonicated salmon sperm (ThermoFisher #AM9680, 200 mg/mL beads) and BSA (NEB #B9000S, 250 mg/mL beads) in dilution buffer (0.5% NP40; 200 mM NaCl; 50 mM Tris pH 8.0; protease inhibitors) for 2 h at room temperature. The chromatin was pre-cleared with 80 µL of blocked beads for 1 h at 4°C. Pre-cleared chromatin was incubated with 5 µg of FRA-1 antibody (Santa Cruz #sc-605) overnight at 4°C, then with 40 µL of blocked beads for further 2 h at 4°C. Control mock immunoprecipitation was performed with blocked beads. The beads were washed 1× with Wash1 (20 mM Tris pH 7.5; 2 mM EDTA pH 8.0; 1% Triton; 0.1% SDS; 150 mM NaCl), 1× with Wash2 (20 mM Tris pH 7.5; 2 mM EDTA pH 8.0; 1% Triton; 0.1% SDS; 500 mM NaCl), 1× with LiCl Wash (20 mM Tris pH 7.5; 1 mM EDTA pH 8.0; 1% NP40; 1% deoxycholate; 250 mM LiCl) and 2× in TE (10 mM Tris pH 7.5; 1 mM EDTA). The immuno-complexes were eluted by two 15 min incubations at 30°C with 100 µL Elution buffer (1% SDS, 100 mM $NaHCO_3$), and de-crosslinked overnight at 65°C in the presence of 10 U RNase A (Ambion #AM9780). The immune-precipitated DNA was then purified with the QIAquick PCR purification kit (Qiagen #28104) according to manufacturer's protocol and analyzed by quantitative real-time PCR.

Statistical analysis

All statistical analyses were performed using R programming language. Statistical differences between groups in the *in vitro* assays were assessed by unpaired two-tailed Student's t tests, unless otherwise specified.

Kaplan–Meier survival curves were produced with GraphPad Prism and P values were generated using the Log-Rank statistics.

Results are presented as mean ± standard deviation (SD), and statistical significance was defined as $P \leq 0.05$ for a 95% confidence interval.

Data and code availability

The accession numbers for data reported in this paper are GEO: GSE137310 (Freiburg BTSCs) and GSE138010 (mouse NSCs). All the code used for data analysis and plots generation will be available at: https://github.com/squatrim/Marques2019.

836 **References**

837 Anders, S., Pyl, P.T., and Huber, W. (2015). HTSeq--a Python framework to work with
838 high-throughput sequencing data. Bioinformatics *31*, 166–169.

839 Andreolas, C., Kalogeropoulou, M., Voulgari, A., and Pintzas, A. (2008). Fra-1
840 regulates vimentin during Ha-RAS-induced epithelial mesenchymal transition in
841 human colon carcinoma cells. Int. J. Cancer *122*, 1745–1756.

842 Annibali, D., Whitfield, J.R., Favuzzi, E., Jauset, T., Serrano, E., Cuartas, I., Redondo-
843 Campos, S., Folch, G., Gonzàlez-Juncà, A., Sodir, N.M., et al. (2014). Myc inhibition is
844 effective against glioma and reveals a role for Myc in proficient mitosis. Nat. Commun.
845 *5*, 1–11.

846 Bakiri, L., MacHo-Maschler, S., Custic, I., Niemiec, J., Guió-Carrión, A., Hasenfuss,
847 S.C., Eger, A., Müller, M., Beug, H., and Wagner, E.F. (2015). Fra-1/AP-1 induces
848 EMT in mammary epithelial cells by modulating Zeb1/2 and TGFβ expression. Cell
849 Death Differ. *22*, 336–350.

850 Bao, S., Wu, Q., McLendon, R.E., Hao, Y., Shi, Q., Hjelmeland, A.B., Dewhirst, M.W.,
851 Bigner, D.D., and Rich, J.N. (2006). Glioma stem cells promote radioresistance by
852 preferential activation of the DNA damage response. Nature *444*, 756–760.

853 Basso, K., Margolin, A.A., Stolovitzky, G., Klein, U., Dalla-Favera, R., and Califano,
854 A. (2005). Reverse engineering of regulatory networks in human B cells. Nat. Genet.
855 *37*, 382–390.

856 Bazzoli, E., Pulvirenti, T., Oberstadt, M.C., Perna, F., Wee, B., Schultz, N., Huse, J.T.,
857 Fomchenko, E.I., Voza, F., Tabar, V., et al. (2012). MEF Promotes Stemness in the
858 Pathogenesis of Gliomas. Cell Stem Cell *11*, 836–844.

859 Belteki, G., Haigh, J., Kabacs, N., Haigh, K., Sison, K., Costantini, F., Whitsett, J.,
860 Quaggin, S.E., and Nagy, A. (2005). Conditional and inducible transgene expression in
861 mice through the combinatorial use of Cre-mediated recombination and tetracycline
862 induction. Nucleic Acids Res. *33*, 1–10.

863 Bhat, K.P.L., Salazar, K.L., Balasubramaniyan, V., Wani, K., Heathcock, L.,
864 Hollingsworth, F., James, J.D., Gumin, J., Diefes, K.L., Kim, S.H., et al. (2011). The
865 transcriptional coactivator TAZ regulates mesenchymal differentiation in malignant

glioma. Genes Dev. *25*, 2594–2609.

Bhat, K.P.L., Balasubramaniyan, V., Vaillant, B., Ezhilarasan, R., Hummelink, K., Hollingsworth, F., Wani, K., Heathcock, L., James, J.D., Goodman, L.D., et al. (2013). Mesenchymal Differentiation Mediated by NF-κB Promotes Radiation Resistance in Glioblastoma. Cancer Cell *24*, 331–346.

Bowman, R.L., Wang, Q., Carro, A., Verhaak, R.G.W., and Squatrito, M. (2017). GlioVis data portal for visualization and analysis of brain tumor expression datasets. Neuro. Oncol. *19*, 139–141.

Brennan, C.W., Verhaak, R.G.W., McKenna, A., Campos, B., Noushmehr, H., Salama, S.R., Zheng, S., Chakravarty, D., Sanborn, J.Z., Berman, S.H., et al. (2013). The somatic genomic landscape of glioblastoma. Cell *155*, 462–477.

Carro, M.S., Lim, W.K., Alvarez, M.J., Bollo, R.J., Zhao, X., Snyder, E.Y., Sulman, E.P., Anne, S.L., Doetsch, F., Colman, H., et al. (2010). The transcriptional network for mesenchymal transformation of brain tumours. Nature *463*, 318–325.

Casalino, L., De Cesare, D., and Verde, P. (2003). Accumulation of Fra-1 in ras-Transformed Cells Depends on Both Transcriptional Autoregulation and MEK-Dependent Posttranslational Stabilization. Mol. Cell. Biol. *23*, 4401–4415.

Castro, M.A.A., de Santiago, I., Campbell, T.M., Vaughn, C., Hickey, T.E., Ross, E., Tilley, W.D., Markowetz, F., Ponder, B.A.J., and Meyer, K.B. (2016). Regulators of genetic risk of breast cancer identified by integrative network analysis. Nat. Genet. *48*, 12–21.

Ceccarelli, M., Barthel, F.P., Malta, T.M., Sabedot, T.S., Salama, S.R., Murray, B.A., Morozova, O., Newton, Y., Radenbaugh, A., Pagnotta, S.M., et al. (2016). Molecular Profiling Reveals Biologically Discrete Subsets and Pathways of Progression in Diffuse Glioma. Cell *164*, 550–563.

Chen, J., Li, Y., Yu, T.S., McKay, R.M., Burns, D.K., Kernie, S.G., and Parada, L.F. (2012). A restricted cell population propagates glioblastoma growth after chemotherapy. Nature *488*, 522–526.

Chiappetta, G., Ferraro, A., Botti, G., Monaco, M., Pasquinelli, R., Vuttariello, E.,

Arnaldi, L., Di Bonito, M., D'Aiuto, G., Pierantoni, G.M., et al. (2007). FRA-1 protein overexpression is a feature of hyperplastic and neoplastic breast disorders. BMC Cancer *7*, 17.

Cooper, L.A.D., Gutman, D.A., Chisolm, C., Appin, C., Kong, J., Rong, Y., Kurc, T., Van Meir, E.G., Saltz, J.H., Moreno, C.S., et al. (2012). The Tumor Microenvironment Strongly Impacts Master Transcriptional Regulators and Gene Expression Class of Glioblastoma. Am. J. Pathol. *180*, 2108–2119.

Debinski, W., and Gibo, D.M. (2005). Fos-related antigen 1 modulates malignant features of glioma cells. Mol. Cancer Res. *3*, 237–249.

Diesch, J., Sanij, E., Gilan, O., Love, C., Tran, H., Fleming, N.I., Ellul, J., Amalia, M., Haviv, I., Pearson, R.B., et al. (2014). Widespread FRA1-Dependent Control of Mesenchymal Transdifferentiation Programs in Colorectal Cancer Cells. PLoS One *9*, 1–11.

Dobin, A., Davis, C.A., Schlesinger, F., Drenkow, J., Zaleski, C., Jha, S., Batut, P., Chaisson, M., and Gingeras, T.R. (2013). STAR: ultrafast universal RNA-seq aligner. Bioinformatics *29*, 15–21.

Eferl, R., and Wagner, E.F. (2003). AP-1: A double-edged sword in tumorigenesis. Nat. Rev. Cancer *3*, 859–868.

Fedele, M., Cerchia, L., Pegoraro, S., Sgarra, R., and Manfioletti, G. (2019). Proneural-Mesenchymal Transition: Phenotypic Plasticity to Acquire Multitherapy Resistance in Glioblastoma. Int. J. Mol. Sci. *20*, 2746.

Fedele, V., Dai, F., Masilamani, A.P., Heiland, D.H., Kling, E., Gätjens-Sanchez, A.M., Ferrarese, R., Platania, L., Soroush, D., Kim, H., et al. (2017). Epigenetic Regulation of ZBTB18 Promotes Glioblastoma Progression. Mol. Cancer Res. *15*, 998–1011.

Fletcher, M.N.C., Castro, M.A.A., Wang, X., de Santiago, I., O'Reilly, M., Chin, S.-F., Rueda, O.M., Caldas, C., Ponder, B.A.J., Markowetz, F., et al. (2013). Master regulators of FGFR2 signalling and breast cancer risk. Nat. Commun. *4*, 2464.

Friedmann-Morvinski, D., Bushong, E.A., Ke, E., Soda, Y., Marumoto, T., Singer, O., Ellisman, M.H., and Verma, I.M. (2012). Dedifferentiation of neurons and astrocytes by

924 oncogenes can induce gliomas in mice. Science *338*, 1080–1084.

925 Gao, X.-Q., Ge, Y.-S., Shu, Q.-H., and Ma, H.-X. (2017). Expression of Fra-1 in human
926 hepatocellular carcinoma and its prognostic significance. Tumour Biol. *39*,
927 1010428317709635.

928 Günther, H.S., Schmidt, N.O., Phillips, H.S., Kemming, D., Kharbanda, S., Soriano, R.,
929 Modrusan, Z., Meissner, H., Westphal, M., and Lamszus, K. (2008). Glioblastoma-
930 derived stem cell-enriched cultures form distinct subgroups according to molecular and
931 phenotypic criteria. Oncogene *27*, 2897–2909.

932 Halliday, J., Helmy, K., Pattwell, S.S., Pitter, K.L., LaPlant, Q., Ozawa, T., and
933 Holland, E.C. (2014). In vivo radiation response of proneural glioma characterized by
934 protective p53 transcriptional program and proneural-mesenchymal shift. Proc. Natl.
935 Acad. Sci. *111*, 5248–5253.

936 Hambardzumyan, D., Amankulor, N.M., Helmy, K.Y., Becher, O.J., and Holland, E.C.
937 (2009). Modeling Adult Gliomas Using RCAS/t-va Technology. Transl. Oncol. *2*, 89–
938 95.

939 Hasenfuss, S.C., Bakiri, L., Thomsen, M.K., Hamacher, R., and Wagner, E.F. (2014).
940 Activator protein 1 transcription factor fos-related antigen 1 (fra-1) is dispensable for
941 murine liver fibrosis, but modulates xenobiotic metabolism. Hepatology *59*, 261–273.

942 Holland, E.C., Celestino, J., Dai, C., Schaefer, L., Sawaya, R.E., and Fuller, G.N.
943 (2000). Combined activation of Ras and Akt in neural progenitors induces glioblastoma
944 formation in mice. Nat. Genet. *25*, 55–57.

945 Koschmann, C., Calinescu, A.-A., Nunez, F.J., Mackay, A., Fazal-Salom, J., Thomas,
946 D., Mendez, F., Kamran, N., Dzaman, M., Mulpuri, L., et al. (2016). ATRX loss
947 promotes tumor growth and impairs nonhomologous end joining DNA repair in glioma.
948 Sci. Transl. Med. *8*, 328ra28.

949 Lau, E.Y.T., Lo, J., Cheng, B.Y.L., Ma, M.K.F., Lee, J.M.F., Ng, J.K.Y., Chai, S., Lin,
950 C.H., Tsang, S.Y., Ma, S., et al. (2016). Cancer-Associated Fibroblasts Regulate
951 Tumor-Initiating Cell Plasticity in Hepatocellular Carcinoma through c-
952 Met/FRA1/HEY1 Signaling. Cell Rep. *15*, 1175–1189.

953 Liu, H., Ren, G., Wang, T., Chen, Y., Gong, C., Bai, Y., Wang, B., Qi, H., Shen, J.,
954 Zhu, L., et al. (2015). Aberrantly expressed Fra-1 by IL-6/STAT3 transactivation
955 promotes colorectal cancer aggressiveness through epithelial-mesenchymal transition.
956 Carcinogenesis *36*, 459–468.

957 Love, M.I., Huber, W., and Anders, S. (2014). Moderated estimation of fold change and
958 dispersion for RNA-seq data with DESeq2. Genome Biol. *15*, 550.

959 Mack, S.C., Singh, I., Wang, X., Hirsch, R., Wu, Q., Villagomez, R., Bernatchez, J.A.,
960 Zhu, Z., Gimple, R.C., Kim, L.J.Y., et al. (2019). Chromatin landscapes reveal
961 developmentally encoded transcriptional states that define human glioblastoma. J. Exp.
962 Med. *216*, 1071–1090.

963 Mani, S.A., Guo, W., Liao, M.-J., Eaton, E.N., Ayyanan, A., Zhou, A.Y., Brooks, M.,
964 Reinhard, F., Zhang, C.C., Shipitsin, M., et al. (2008). The epithelial-mesenchymal
965 transition generates cells with properties of stem cells. Cell *133*, 704–715.

966 Mansuy, I.M., and Bujard, H. (2000). Tetracycline-regulated gene expression in the
967 brain. Curr. Opin. Neurobiol. *10*, 593–596.

968 Mao, P., Joshi, K., Li, J., Kim, S.-H., Li, P., Santana-Santos, L., Luthra, S., Chandran,
969 U.R., Benos, P. V., Smith, L., et al. (2013). Mesenchymal glioma stem cells are
970 maintained by activated glycolytic metabolism involving aldehyde dehydrogenase 1A3.
971 Proc. Natl. Acad. Sci. *110*, 8644–8649.

972 McCormick, F. (1990). GAP as ras effector or negative regulator? Mol. Carcinog. *3*,
973 185–187.

974 Muñoz, D.M., Tung, T., Agnihotri, S., Singh, S., Guha, A., Zadeh, G., and Hawkins, C.
975 (2013). Loss of p53 cooperates with K-ras activation to induce glioma formation in a
976 region-independent manner. Glia *61*, 1862–1872.

977 Neftel, C., Laffy, J., Filbin, M.G., Hara, T., Shore, M.E., Rahme, G.J., Richman, A.R.,
978 Silverbush, D., Shaw, M.L., Hebert, C.M., et al. (2019). An Integrative Model of
979 Cellular States, Plasticity, and Genetics for Glioblastoma. Cell *178*, 835-849.e21.

980 Oldrini, B., Curiel-García, Á., Marques, C., Matia, V., Uluçkan, Ö., Graña-Castro, O.,
981 Torres-Ruiz, R., Rodriguez-Perales, S., Huse, J.T., and Squatrito, M. (2018). Somatic

genome editing with the RCAS-TVA-CRISPR-Cas9 system for precision tumor modeling. Nat. Commun. *9*, 1466.

Ozawa, T., Riester, M., Cheng, Y.K., Huse, J.T., Squatrito, M., Helmy, K., Charles, N., Michor, F., and Holland, E.C. (2014). Most human non-GCIMP glioblastoma subtypes evolve from a common proneural-like precursor glioma. Cancer Cell *26*, 288–300.

Patel, A.P., Tirosh, I., Trombetta, J.J., Shalek, A.K., Gillespie, S.M., Wakimoto, H., Cahill, D.P., Nahed, B. V, Curry, W.T., Martuza, R.L., et al. (2014). Single-cell RNA-seq highlights intratumoral heterogeneity in primary glioblastoma. Science *344*, 1396–1401.

Phillips, H.S., Kharbanda, S., Chen, R., Forrest, W.F., Soriano, R.H., Wu, T.D., Misra, A., Nigro, J.M., Colman, H., Soroceanu, L., et al. (2006). Molecular subclasses of high-grade glioma predict prognosis, delineate a pattern of disease progression, and resemble stages in neurogenesis. Cancer Cell *9*, 157–173.

Ricci-Vitiani, L., Pallini, R., Larocca, L.M., Lombardi, D.G., Signore, M., Pierconti, F., Petrucci, G., Montano, N., Maira, G., and De Maria, R. (2008). Mesenchymal differentiation of glioblastoma stem cells. Cell Death Differ. *15*, 1491–1498.

Sandberg, C.J., Altschuler, G., Jeong, J., Strømme, K.K., Stangeland, B., Murrell, W., Grasmo-Wendler, U.H., Myklebost, O., Helseth, E., Vik-Mo, E.O., et al. (2013). Comparison of glioma stem cells to neural stem cells from the adult human brain identifies dysregulated Wnt- signaling and a fingerprint associated with clinical outcome. Exp. Cell Res. *319*, 2230–2243.

Sottoriva, A., Spiteri, I., Piccirillo, S.G.M., Touloumis, A., Collins, V.P., Marioni, J.C., Curtis, C., Watts, C., and Tavare, S. (2013). Intratumor heterogeneity in human glioblastoma reflects cancer evolutionary dynamics. Proc. Natl. Acad. Sci. *110*, 4009–4014.

Subramanian, A., Tamayo, P., Mootha, V.K., Mukherjee, S., Ebert, B.L., Gillette, M.A., Paulovich, A., Pomeroy, S.L., Golub, T.R., Lander, E.S., et al. (2005). Gene set enrichment analysis: a knowledge-based approach for interpreting genome-wide expression profiles. Proc. Natl. Acad. Sci. U. S. A. *102*, 15545–15550.

Tam, W.L., and Weinberg, R.A. (2013). The epigenetics of epithelial-mesenchymal

plasticity in cancer. Nat. Med. *19*, 1438–1449.

Tam, W.L., Lu, H., Buikhuisen, J., Soh, B.S., Lim, E., Reinhardt, F., Wu, Z.J., Krall, J.A., Bierie, B., Guo, W., et al. (2013). Protein kinase C alpha is a central signaling node and therapeutic target for breast cancer stem cells. Cancer Cell *24*, 347–364.

The Cancer Genome Atlas Research Network (2008). Comprehensive genomic characterization defines human glioblastoma genes and core pathways. Nature *455*, 1061–1068.

Tso, C.-L., Shintaku, P., Chen, J., Liu, Q., Liu, J., Chen, Z., Yoshimoto, K., Mischel, P.S., Cloughesy, T.F., Liau, L.M., et al. (2006). Primary Glioblastomas Express Mesenchymal Stem-Like Properties. Mol. Cancer Res. *4*, 607–619.

Uhrbom, L., Dai, C., Celestino, J.C., Rosenblum, M.K., Fuller, G.N., and Holland, E.C. (2002). Ink4a-Arf loss cooperates with KRas activation in astrocytes and neural progenitors to generate glioblastomas of various morphologies depending on activated Akt. Cancer Res. *62*, 5551–5558.

Usui, A., Hoshino, I., Akutsu, Y., Sakata, H., Nishimori, T., Murakami, K., Kano, M., Shuto, K., and Matsubara, H. (2012). The molecular role of Fra-1 and its prognostic significance in human esophageal squamous cell carcinoma. Cancer *118*, 3387–3396.

Vallejo, A., Perurena, N., Guruceaga, E., Mazur, P.K., Martinez-Canarias, S., Zandueta, C., Valencia, K., Arricibita, A., Gwinn, D., Sayles, L.C., et al. (2017). An integrative approach unveils FOSL1 as an oncogene vulnerability in KRAS-driven lung and pancreatic cancer. Nat. Commun. *8*.

Verde, P., Casalino, L., Talotta, F., Yaniv, M., and Weitzman, J.B. (2007). Deciphering AP-1 function in tumorigenesis: fra-ternizing on target promoters. Cell Cycle *6*, 2633–2639.

Verhaak, R.G.W., Hoadley, K.A., Purdom, E., Wang, V., Qi, Y., Wilkerson, M.D., Miller, C.R., Ding, L., Golub, T., Mesirov, J.P., et al. (2010). Integrated Genomic Analysis Identifies Clinically Relevant Subtypes of Glioblastoma Characterized by Abnormalities in PDGFRA, IDH1, EGFR, and NF1. Cancer Cell *17*, 98–110.

Wang, J., Cazzato, E., Ladewig, E., Frattini, V., Rosenbloom, D.I.S., Zairis, S., Abate,

F., Liu, Z., Elliott, O., Shin, Y.-J., et al. (2016). Clonal evolution of glioblastoma under therapy. Nat. Genet. *48*, 768–776.

Wang, L., Babikir, H., Muller, S., Yagnik, G., Shamardani, K., Catalan, F., Kohanbash, G., Alvarado, B., Di Lullo, E., Kriegstein, A., et al. (2019). The phenotypes of proliferating glioblastoma cells reside on a single axis of variation. Cancer Discov. CD-19-0329.

Wang, Q., Hu, B., Hu, X., Kim, H., Squatrito, M., Scarpace, L., deCarvalho, A.C., Lyu, S., Li, P., Li, Y., et al. (2017). Tumor Evolution of Glioma-Intrinsic Gene Expression Subtypes Associates with Immunological Changes in the Microenvironment. Cancer Cell *32*, 42-56.e6.

Wu, J., Ji, A., Wang, X., Zhu, Y., Yu, Y., Lin, Y., Liu, Y., Li, S., Liang, Z., Xu, X., et al. (2015). MicroRNA-195-5p, a new regulator of Fra-1, suppresses the migration and invasion of prostate cancer cells. J. Transl. Med. *13*, 289.

Xu, H., Jin, X., Yuan, Y., Deng, P., Jiang, L., Zeng, X., Li, X.-S., Wang, Z.-Y., and Chen, Q.-M. (2017). Prognostic value from integrative analysis of transcription factors c-Jun and Fra-1 in oral squamous cell carcinoma: a multicenter cohort study. Sci. Rep. *7*, 7522.

Ye, X., Tam, W.L., Shibue, T., Kaygusuz, Y., Reinhardt, F., Ng Eaton, E., and Weinberg, R.A. (2015). Distinct EMT programs control normal mammary stem cells and tumour-initiating cells. Nature *525*, 256–260.

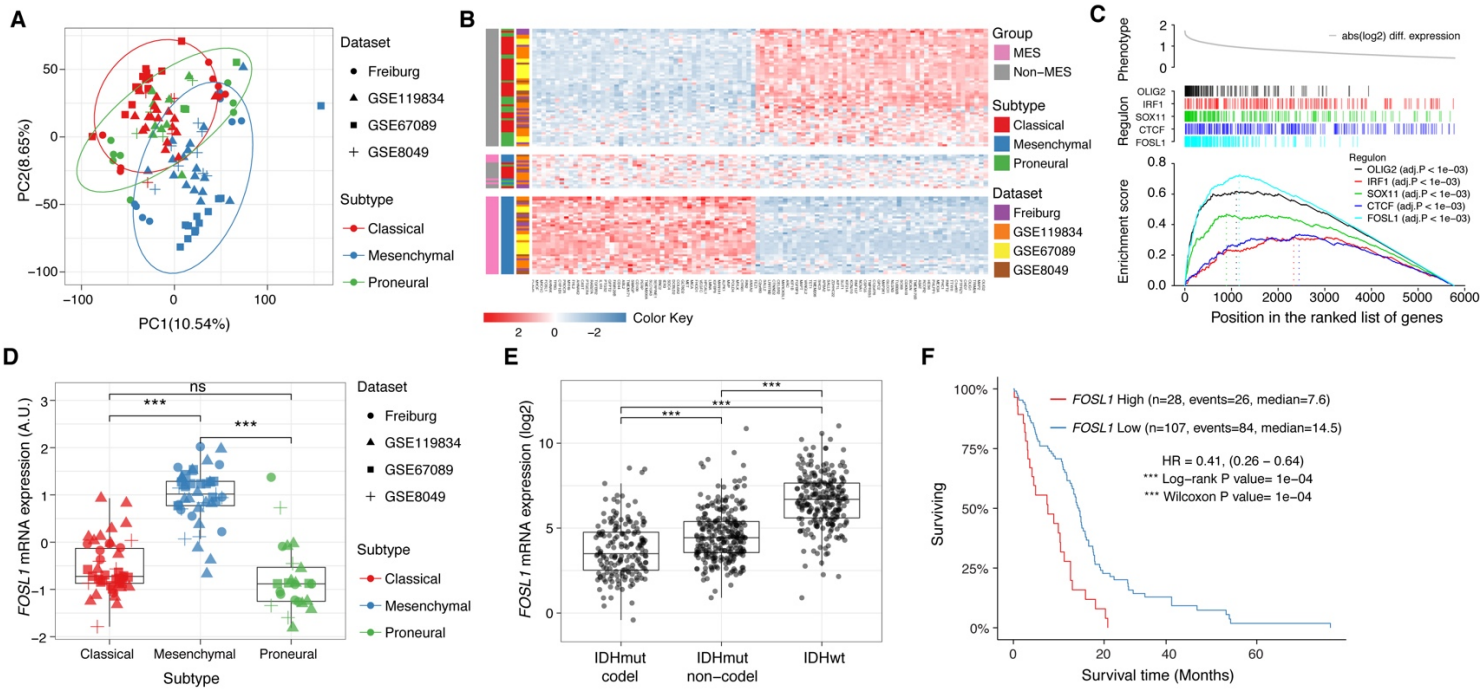

Figure 1. *FOSL1* is a master regulator of the glioma-intrinsic MES transcriptional signature. A) Principal Component (PC) analysis of the BTSCs expression dataset. **B)** Heatmap of the top 100 differentially expressed genes between MES and Non-MES BTSCs. **C)** One-tail GSEA of the top 5 scoring TFs in the MRA. **D)** *FOSL1* mRNA expression in the BTSCs dataset. Student's t test, *P ≤ 0.05, ***P ≤ 0.001. **E)** *FOSL1* mRNA expression in the TCGA dataset. Tumors were separated according to their molecular subtype classification. Student's t test, ***P ≤ 0.001. **F)** Kaplan-Meier survival curves of the IDH-wt GBM TCGA tumors stratified based on *FOSL1* expression. *See also Figure S1*.

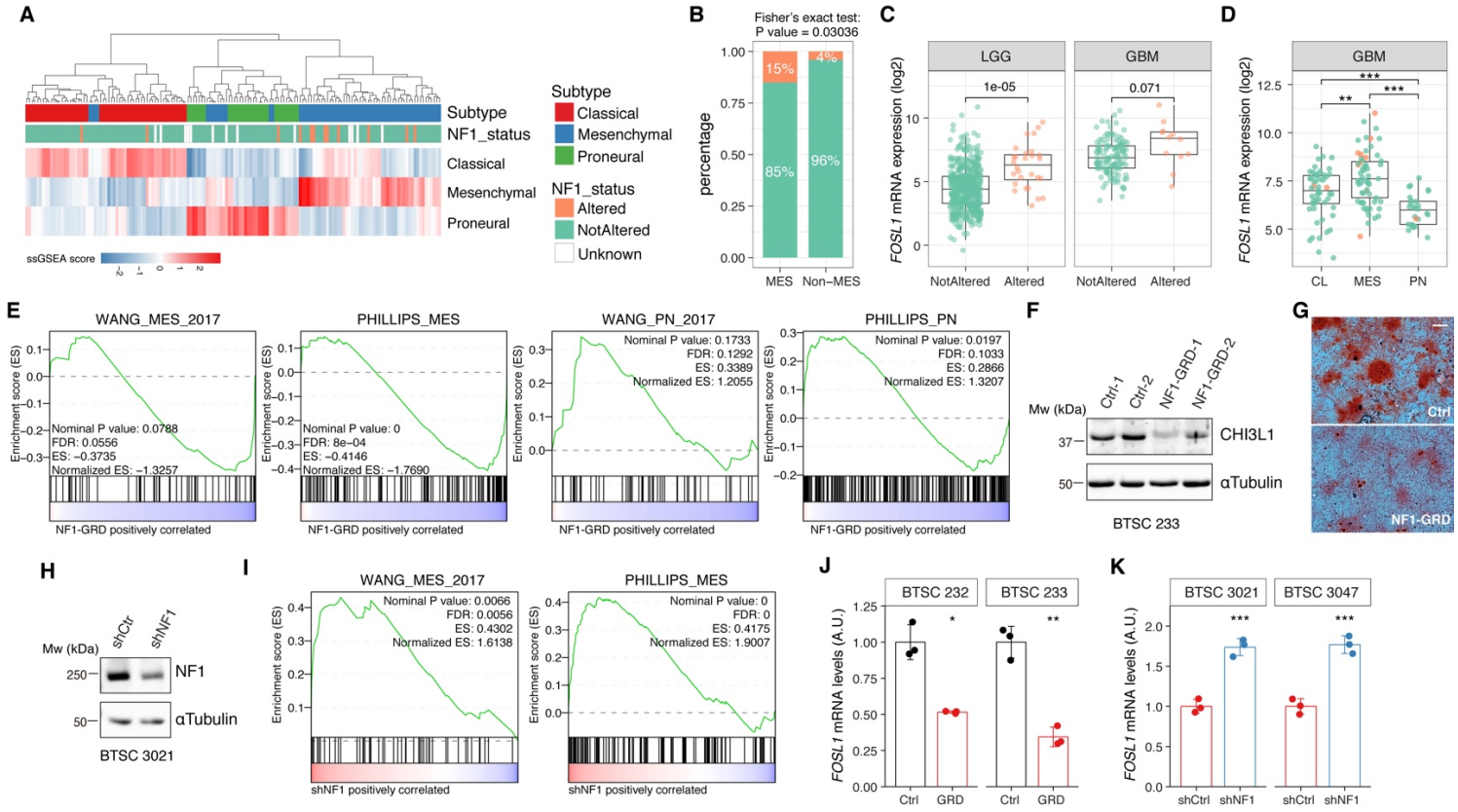

Figure 2. *NF1* is a functional modulator of MES transcriptional signature and *FOSL1* expression. A) Heatmap of the subtype ssGSEA scores and *NF1* genetic alterations of the IDH-wt GBM TCGA tumors. **B)** Frequency of *NF1* alterations in MES and Non-MES GBMs. Colors are as in panel A. **C)** and **D)** *FOSL1* mRNA expression in the TCGA dataset. Tumors were separated according to either *NF1* alterations (C) or transcriptional subtypes (D). Colors are as in panel A. Student's t test, **P ≤ 0.01, ***P ≤ 0.001. **E)** GSEA of BTSC 233 MES cells transduced with NF1-GRD expressing lentivirus versus Ctrl. Gene signatures from Wang and Phillips studies were analyzed (MES, *left panels*; PN, *right panels*). ES = Enrichment score. **F)** Western blot analysis of whole-cell-extract of BTSC 233 cells showing CHI3L1 mesenchymal marker expression upon NF1-GRD transduction. Tubulin was used as loading control. **G)** Osteogenesis differentiation assay of BTSC 233 transduced as indicated above. Alzarin Red staining indicates osteogenesis differentiation. Scale bar represents 200 µm. **H)** Western blot analysis of whole-cell-extract of proneural BTSC 3021 cells transduced with either *NF1* (sh*NF1*) or control (shCtrl) shRNAs. **I)** GSEA of BTSC 3021 transduced with sh*NF1* versus Ctrl. **J)** and **K)** qRT-PCR analysis of *FOSL1* expression upon NF1-GRD overexpression in BTSC 232 and BTSC 233 cells (J) or NF1 knockdown in 3021 and 3047 cells (K). Data are presented as mean ± SD (n=3), normalized to 18s rRNA expression; Student's t test, *P ≤ 0.05, **P ≤ 0.01, ***P ≤ 0.001. *See also Figure S2-S3*.

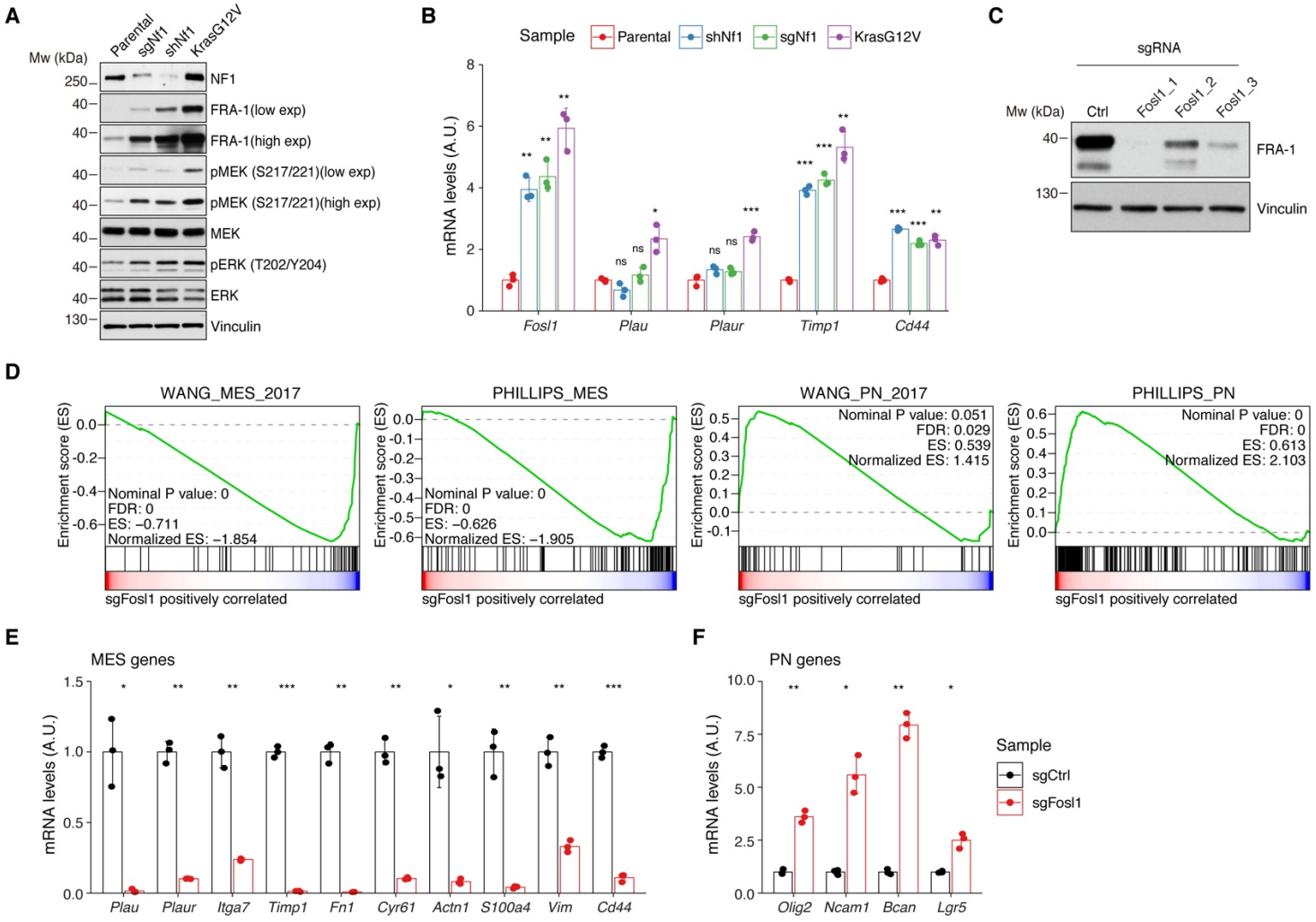

Figure 3. *Fosl1* is induced by MAPK kinase activation and is required for MES gene expression. A) Western blot analysis using the specified antibodies of p53-null NSCs, parental and infected with sg*Nf1*, sh*Nf1* and *Kras*^{G12V}; Vinculin used as loading control. **B)** mRNA expression of *Fosl1* and MES genes (*Plau, Plaur, Timp1* and *Cd44*), in infected p53-null NSCs, compared to parental cells (not infected). Data from a representative of two experiments are presented as mean ± SD (n=3), normalized to *Gapdh* expression. Student's t test, relative to parental cells: ns = not significant, *P ≤ 0.05, **P ≤ 0.01, ***P ≤ 0.001. **C)** FRA-1 expression detected by Western blot in p53-null *Kras*^{G12V} NSCs upon transduction with sgRNAs targeting *Fosl1*, after selection with 1 µg/mL puromycin; Vinculin used as loading control. **D)** GSEA of p53-null *Kras*^{G12V} sg*Fosl1*_1 versus sgCtrl NSCs. Gene signatures from Wang and Phillips studies were analyzed (MES, *left panels*; PN, *right panels*). **E)** and **F)** mRNA expression of MES and PN genes, respectively, in sgCtrl and sg*Fosl1*_1 p53-null *Kras*^{G12V} NSCs. Data from a representative of two experiments are presented as mean ± SD (n=3), normalized to *Gapdh* expression. Student's t test, relative to sgCtrl: *P ≤ 0.05; **P ≤ 0.01; ***P ≤ 0.001.

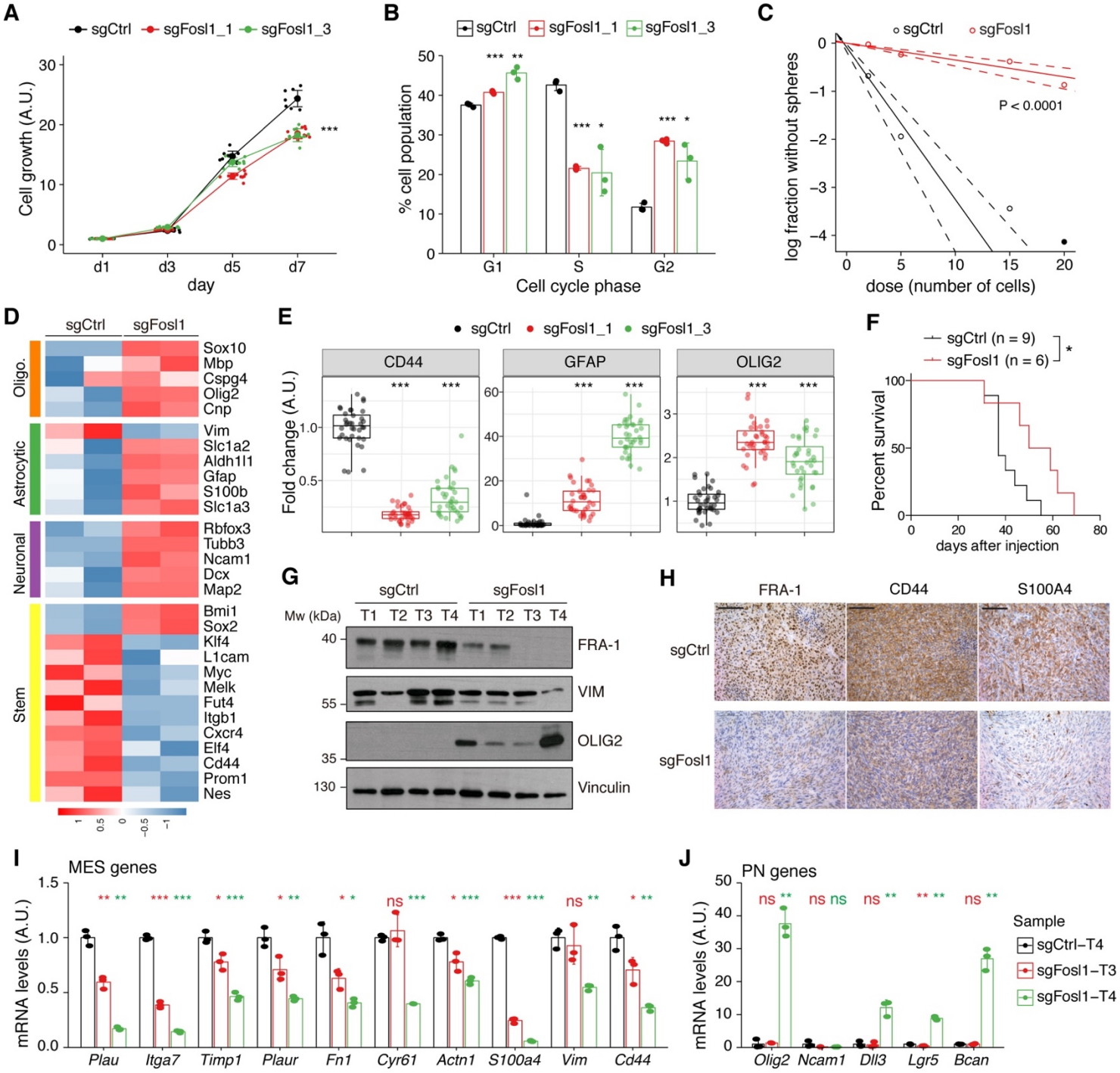

Figure 4. *Fosl1* knock-out impairs cell growth and stemness *in vitro* and increases survival in a xenograft model. A) Cell viability of control and *Fosl1* KO p53-null *Kras*^{G12V} NSCs measured by MTT assay; absorbance values were normalized to day 1. Data from a representative of three independent experiments are presented as mean ± SD (n=10). Student's t test on day 7, relative to sgCtrl: ***P ≤ 0.001. **B)** Quantification of cell cycle populations of control and *Fosl1* KO p53-null *Kras*^{G12V} NSCs by flow cytometry analysis of PI staining. Data from a representative of two independent experiments are presented as mean ± SD (n=3). Student's t test, relative to sgCtrl: *P ≤ 0.05; **P ≤ 0.01; ***P ≤ 0.001. **C)** A representative limiting dilution experiment on p53-null *Kras*^{G12V} sgCtrl and sg*Fosl1*_1 NSCs, calculated with extreme limiting dilution assay (ELDA) analysis; P < 0.0001. **D)** Heatmap of expression of stem cell (yellow) and lineage-specific (neuronal – purple, astrocytic – green and oligodendrocytic – orange) genes, comparing sgCtrl and sg*Fosl1*_1 p53-null *Kras*^{G12V} NSCs. **E)** Quantification of pixel area (fold change

relative to sgCtrl) of CD44, GFAP and OLIG2 relative to DAPI pixel area per field of view in control and *Fosl1* KO p53-null *Kras*^{G12V} NSCs. Data from a representative of two independent experiments; Student's t test, relative to sgCtrl: ***P ≤ 0.001. **F)** Kaplan-Meier survival curves of *nu*/*nu* mice injected with p53-null *Kras*^{G12V} sgCtrl (n=9) and sg*Fosl1*_1 (n=6) NSCs. Log-rank P = 0.0263. **G)** Western blot analysis using the indicated antibodies of 4 sgCtrl and 4 sg*Fosl1*_1 tumors (showing low or no detectable expression of FRA-1); Vinculin used as loading control. **H)** Representative images of IHCs using the indicated antibodies. Scale bars represent 100 µm. **I)** mRNA expression of MES genes in the samples sgCtrl–T4 (higher FRA-1 expression) and sg*Fosl1*_1–T3 and –T4 (no detectable FRA-1 expression). **J)** mRNA expression of PN genes in samples as in (H). Data from a representative of two experiments are presented as mean ± SD (n=3), normalized to *Gapdh* expression. Student's t test for sg*Fosl1*_1 tumors, relative to sgCtrl–T4: ns = not significant, *P ≤ 0.05, **P ≤ 0.01, ***P ≤ 0.001. *See also Figure S4*.

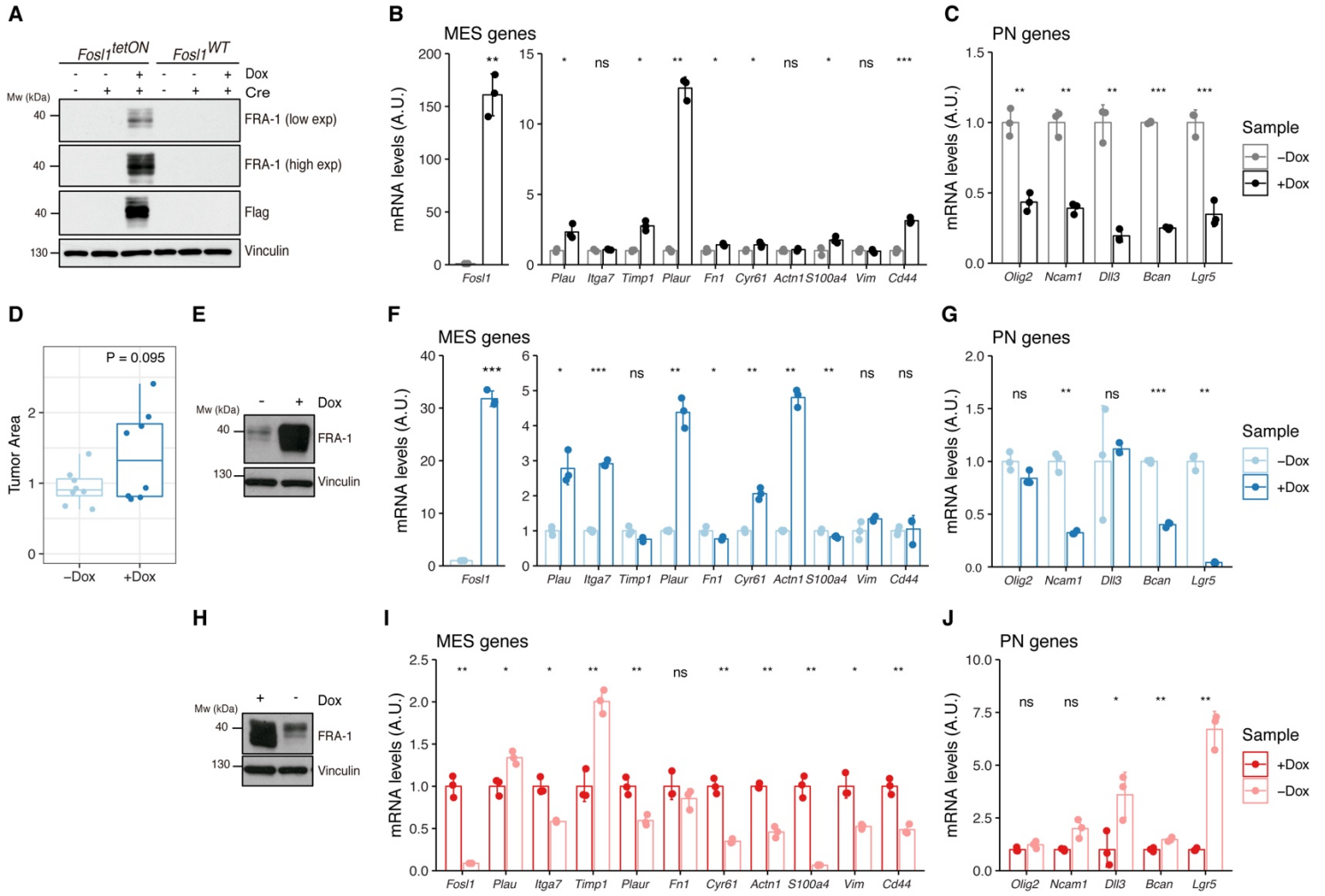

Figure 5. ***Fosl1*** **overexpression upregulates the MGS and induces larger tumors** ***in vivo*****. A)** Western blot analysis of FRA-1 and Flag expression on *Fosl1*^{tetON} and *Fosl1*^{WT} NSCs derived from *Kras*^{LSLG12V}*; Trp53*^{lox}*; ROSA26*$^{LSLrtTA\text{-}IRES\text{-}EGFP}$*; Col1a1*$^{TetO\text{-}Fosl1}$ mice, upon *in vitro* infection with Cre and induction of *Fosl1* overexpression with 1 µg/mL Dox for 72 h; Vinculin used as loading control. **B)** mRNA expression of *Fosl1* and MES genes in *Fosl1*^{tetON} p53-null *Kras*^{G12V} cells upon 72 h induction with 1 µg/mL Dox. **C)** mRNA expression of PN genes in *Fosl1*^{tetON} p53-null *Kras*^{G12V} cells upon 72 h induction with 1 µg/mL Dox. **D)** Quantification of tumor area (µm^2) of –Dox and +Dox tumors (n=8/8). For each mouse, the brain section on the H&E slide with a larger tumor was considered and quantified using the ZEN software (Zeiss). **E)** Western blot detection of FRA-1 expression in tumorspheres derived from a control (−Dox) tumor. Tumorspheres were isolated and kept without Dox until first passage, when 1 µg/mL Dox was added and kept for 19 days (+Dox *in vitro*). **F)** mRNA expression of *Fosl1* and MES genes in tumorspheres in absence or presence of Dox for 19 days. **G)** mRNA expression of PN genes in tumorspheres in absence or presence of Dox for 19 days. **H)** Western blot detection of FRA-1 expression in tumorspheres derived from a *Fosl1* overexpressing (+Dox) tumor. Tumorspheres were isolated and kept with 1 µg/mL Dox until first passage, when Dox was removed for 19 days (−Dox *in vitro*). **I)** mRNA expression of *Fosl1* and MES genes in tumorspheres in presence or absence of Dox for 19 days. **J)** mRNA expression of PN genes in tumorspheres in presence or absence of Dox for 19 days. qPCR data from a representative of two experiments are presented as mean ± SD (n=3), normalized to *Gapdh* expression. Student's t test, relative to the respective control (−Dox in B, C, F and G; +Dox in I and J): ns = not significant, *P ≤ 0.05, **P ≤ 0.01, ***P ≤ 0.001. *See also Figure S5*.

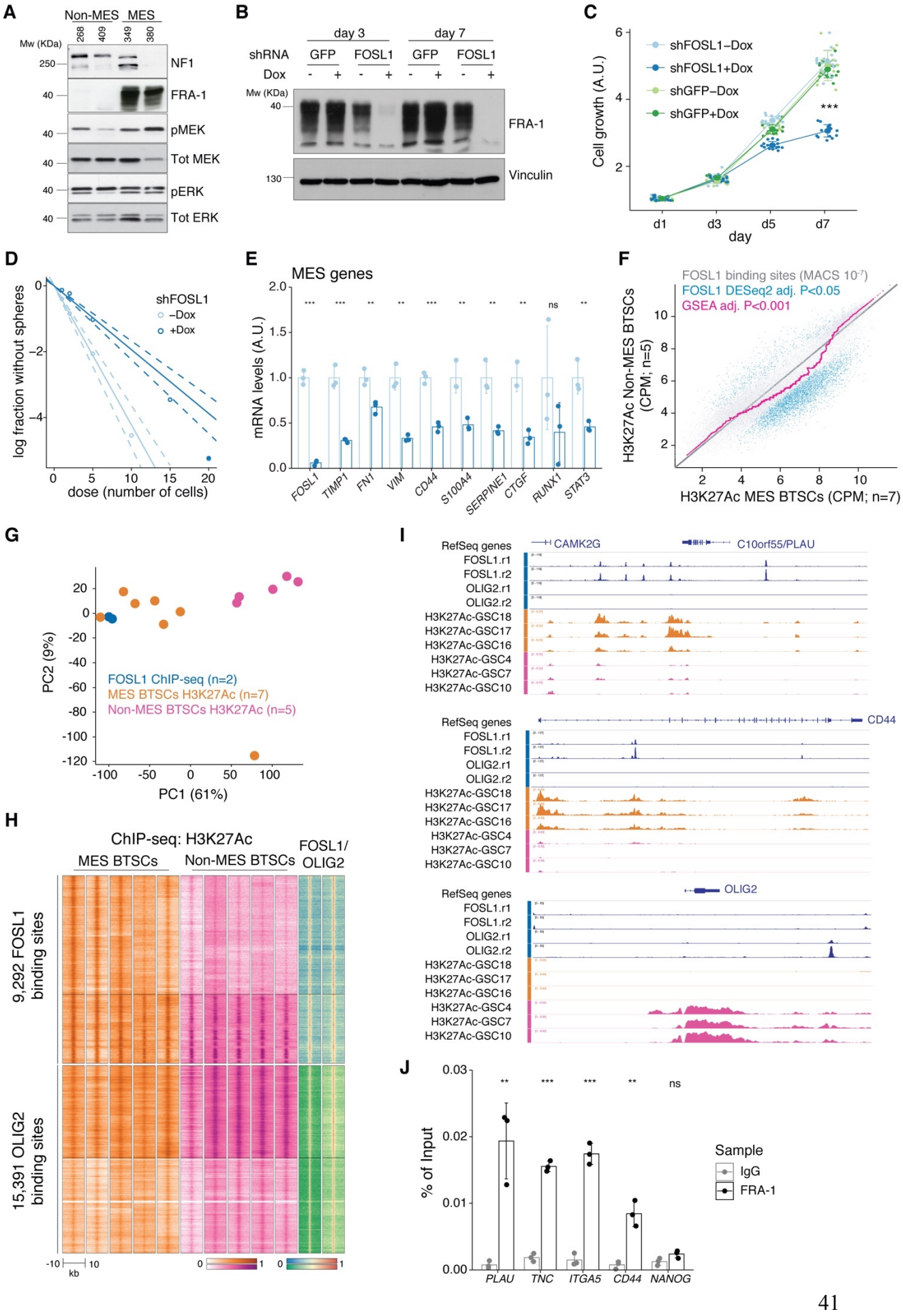

Figure 6. *FOSL1* silencing in a patient-derived MES tumor stem cell line decreases cell growth, stemness and MGS *in vitro*. A) Western blot analysis using the specified antibodies of human brain tumor stem cell lines, characterized as Non-MES (*left*) and MES (*right*). **B)** Western blot detection of FRA-1 in MES BTSC 349 upon transduction with inducible shRNAs targeting GFP (control) and *FOSL1*, analyzed after 3 and 7 days of Dox treatment; Vinculin used as loading control. **C)** Cell growth of BTSC 349 shGFP and sh*FOSL1*, in absence or presence of Dox, measured by MTT assay; absorbance values were normalized to day 1. Data from a representative of three independent experiments are presented as mean ± SD (n=15). Student's t test on day 7, relative to sh*FOSL1* –Dox: ***P ≤ 0.001. **D)** Representative limiting dilution analysis on BTSC 349 sh*FOSL1*, in presence or absence of Dox, calculated with extreme limiting dilution assay (ELDA) analysis; P < 0.0001. **E)** mRNA expression of *FOSL1* and MES genes in BTSC 349 sh*FOSL1* in absence or presence of Dox for 3 days. Data from a representative of three experiments are presented as mean ± SD (n=3), normalized to *GAPDH* expression. Student's t test, relative to –Dox: ns = not significant, *P ≤ 0.05, **P ≤ 0.01, ***P ≤ 0.001. **F)** Scatter plot of H3K27Ac signal for Non-Mes and MES BTSCs (from Mack et al., 2019) on *FOSL1*/FRA-1 peaks calculated using MACS on ENCODE samples (see methods). Blue probes represent statistically significant difference in H3K27Ac signal between Non-Mes and MES BTSCs. Violet trendline indicates a custom regression calculated by a Kolmorogov-Smirnov test, adj-P < 0.05, z > 0.5. **G)** Principal component analysis of H3K27Ac of *FOSL1*/FRA-1 enrichment over *FOSL1*/FRA-1 binding sites for the indicated samples. **H)** Heatmap of ChIP-seq enrichment of *FOSL1*/FRA-1 or OLIG2 binding sites for the indicated profiles. **I)** IGV browser view of the *PLAU*, *CD44* and *OLIG2* loci of selected profiles. **J)** Representative ChIP experiment in BTSC 349 cells. The panel shows FRA-1 binding to the promoter of a subset of mesenchymal targets (n=3 PCR replicates) expressed as percentage of the initial DNA amount in the immune-precipitated fraction. *NANOG* gene was used as a negative control. Student's t test, relative to IgG: ns = not significant, **P ≤ 0.01, ***P ≤ 0.001. *See also Figure S6.*

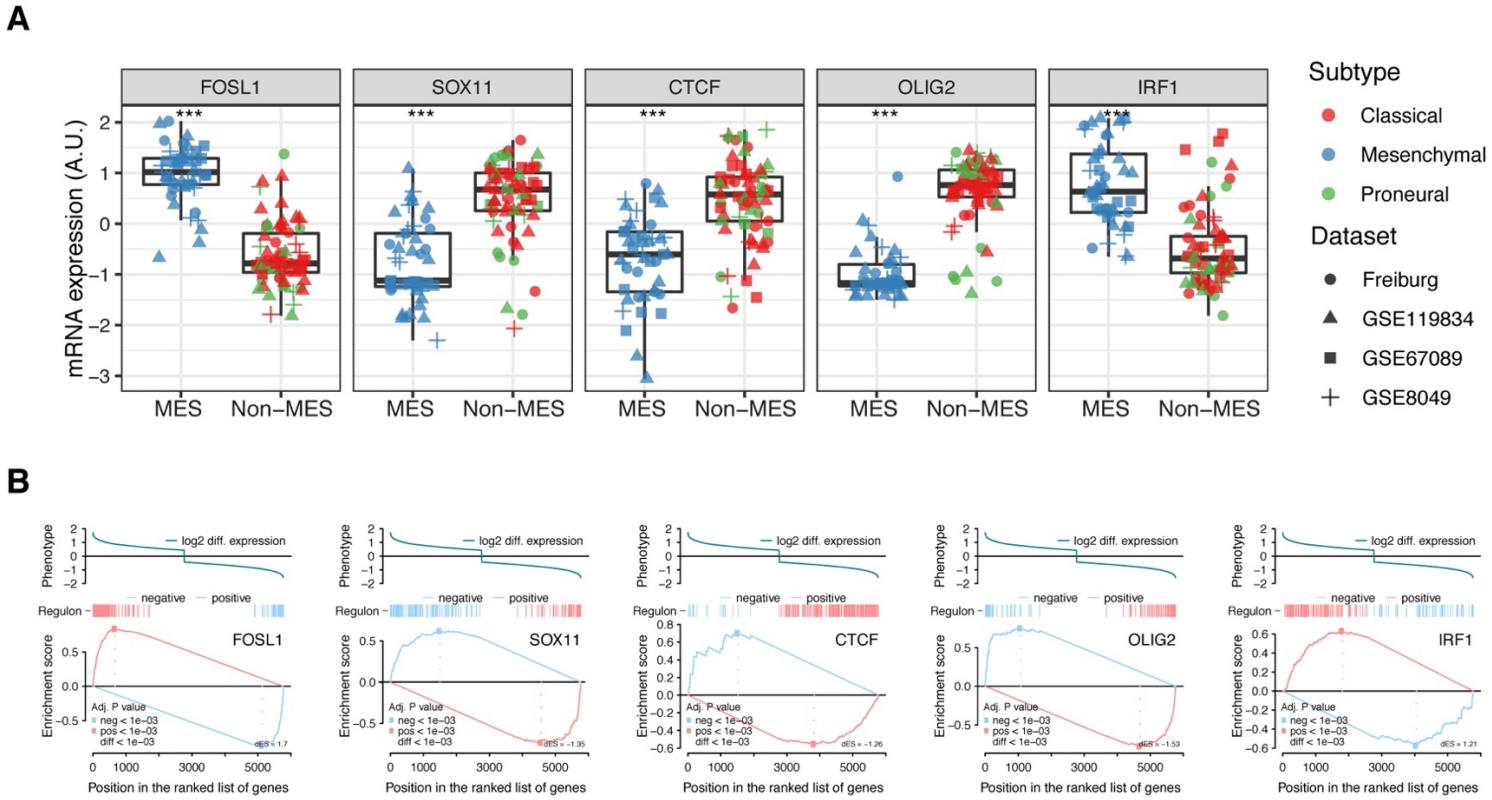

Figure S1. Related to Figure 1. A) mRNA expression of the top 5 scoring TFs in the MRA of the BTSCs dataset, comparing MES versus Non-MES. Student's t test, ***P ≤ 0.001. **B)** Two-tailed GSEA showing positive or negative targets for the top 5 TFs in the MRA ranked by their differential expression (MES vs Non-MES).

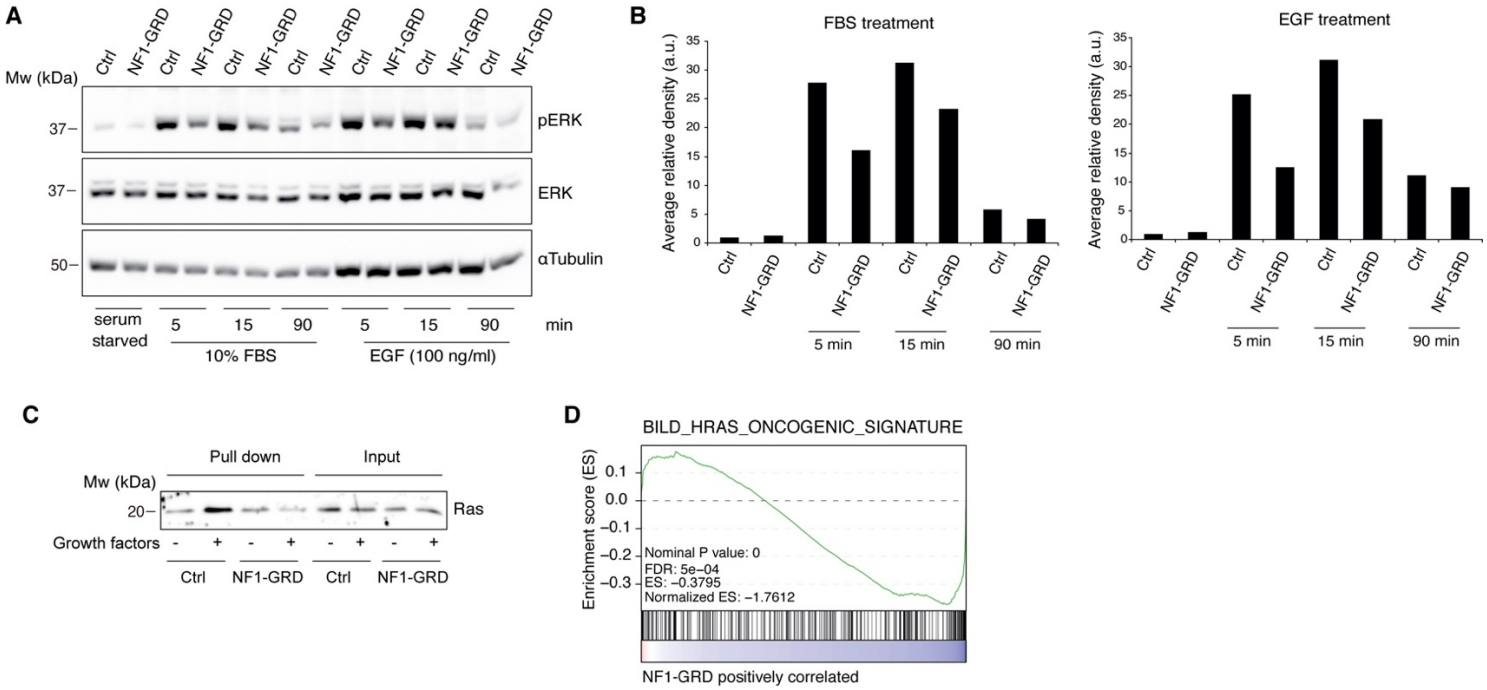

Figure S2. Related to Figure 2. A) Western blot analysis of ERK and pERK expression in BTSC 233 cells transduced with NF1-GRD expressing lentivirus and stimulated with 10% FBS or 100 ng/ml EGF. α-Tubulin is included as loading control. **B)** Densitometric analysis of western blot in A). **C)** Western blot analysis of active Ras pull down assay in BTSC 233 expressing NF1-GRD or control, in presence or absence of growth factors. **D)** GSEA of Ras-induced oncogenic signature in BTSC 233 MES cells transduced with NF1-GRD expressing lentivirus versus Ctrl.

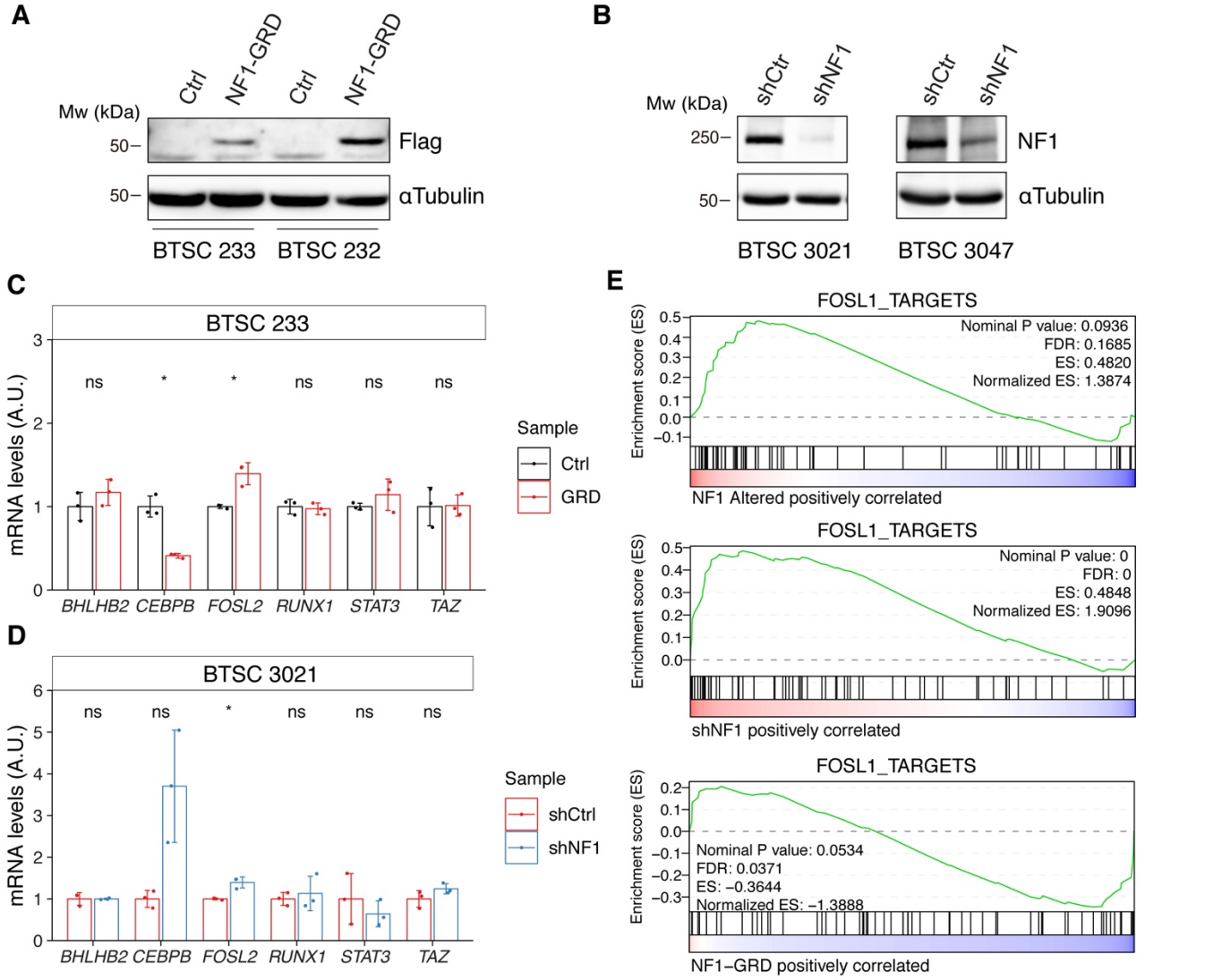

Figure S3. Related to Figure 2. A) Western blot analysis of FLAG-NF1-GRD expression in MES cells (BTSC 233 and 232). **B)** Western blot analysis of NF1 expression upon *NF1* knockdown in PN cells (BTSC 3021 and 3047). **C)** and **D)** qRT-PCR analysis of mesenchymal genes master regulators expression (*BHLHB2*, *CEBPB*, *FOSL2*, *RUNX1*, *STAT3* and *TAZ*) upon NF1-GRD overexpression in BTSC 233 (C) or *NF1* knockdown in 3021 cells (D). Data are presented as mean ± SD (n=3), normalized to GAPDH or 18s rRNA expression; Student's t test, ns = not significant, *P ≤ 0.05. **E)** GSEA of *FOSL1* targets signature in GBMs with *NF1* alteration or wt status (*top panel*), BTSC 3021 cells transduced with sh*NF1* or shCtrl (*middle panel*), and BTSC 233 cells transduced with NF1-GRD or Ctrl vector (*bottom panel*). **F)** and **G)** qRT-PCR analysis of known mesenchymal *FOSL1* targets (*ITGA3*, *ITGA5*, *PLAU*, *SERPINE1* and *TNC*) in BTSC 233 and 232 cells transduced with NF1-GRD expressing lentivirus (F) and BTSC 3021 and 3047 cells transduced with sh*NF1* expressing lentivirus. Data are presented as mean ± SD (n=3), normalized to 18s rRNA expression; Student's t test, ns = not significant, *P ≤ 0.05, **P ≤ 0.01, ***P ≤ 0.001.

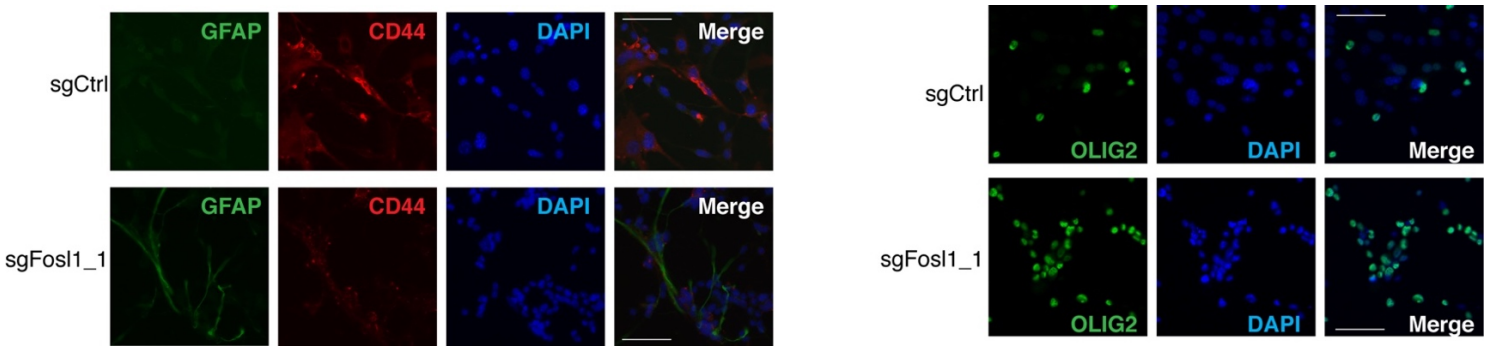

Figure S4. Related to Figure 4. Representative images of immunofluorescence staining of the indicated markers in sgCtrl and sg*Fosl1*_1 p53-null *Kras*^{G12V} NSCs plated on laminin-coated coverslips. Scale bars represent 50 μm.

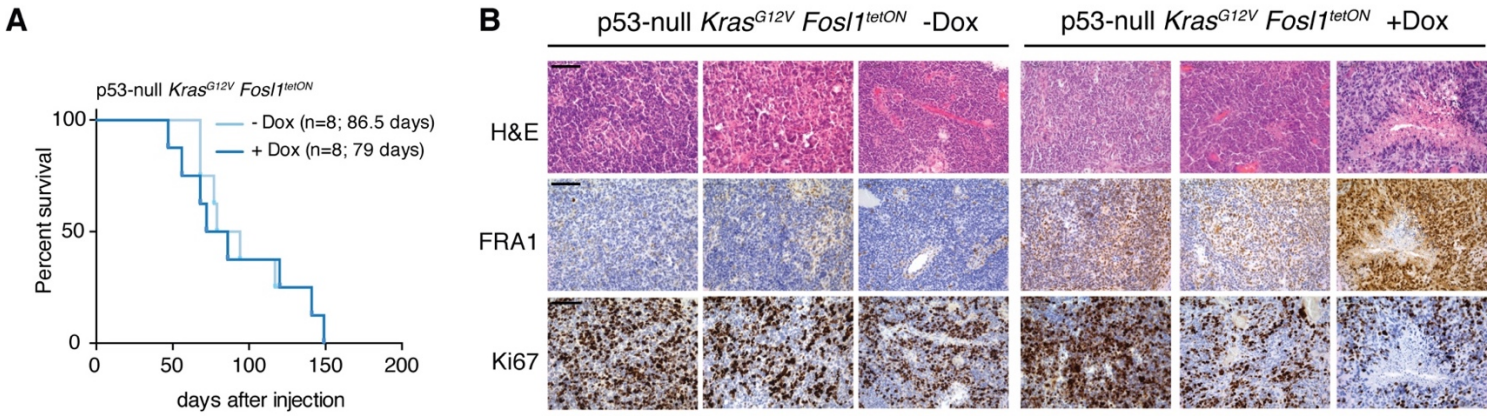

Figure S5. Related to Figure 5. A) Kaplan-Meier survival curves of C57BL/6J wildtype mice injected with p53-null *Kras*^{G12V} *Fosl1*^{tetON} NSCs subjected to Dox diet (n=8) or kept as controls (n=8); Log-rank P value = 0.814. **B)** Hematoxylin and eosin (H&E) and immunohistochemical staining, using the indicated antibodies, of representative –Dox and +Dox tumors. Scale bars represent 100 µm.

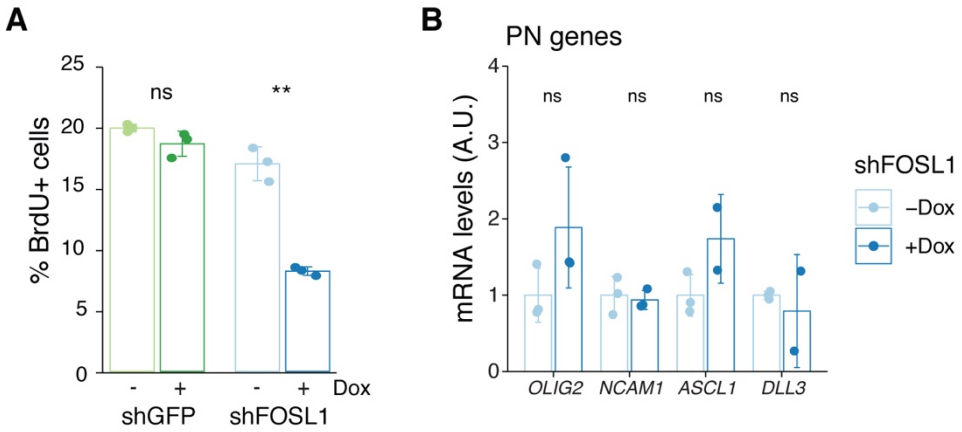

Figure S6. Related to Figure 6. A) BrdU incorporation of BTSC 349 shGFP and sh*FOSL1*, in absence or presence of Dox, analyzed by flow cytometry. Data from a representative of two independent experiments are presented as mean ± SD (n=3). Student's t test, relative to the respective control (–Dox): ns = not significant, **P ≤ 0.01. **B)** mRNA expression of PN genes in BTSC 349 sh*FOSL1* in absence or presence of Dox for 3 days. Data from a representative of three experiments are presented as mean ± SD (n=3), normalized to *GAPDH* expression. Student's t test, relative to –Dox: ns = not significant, *P ≤ 0.05.